# The exhumation history of the middle Hsuehshan Range, Taiwan, as revealed by zircon thermochronological modeling

# The exhumation history of the middle Hsuehshan Range, Taiwan, as revealed by zircon thermochronological modeling

**Chase J. Shyu[1], Eh Tan[2], Linda A. Kirstein[3], Finlay M. Stuart[4], and Yue-Gau Chen[5,6]**

[1]Taiwan International Graduate Program (TIGP) - Earth System Science Program, Academia Sinica and National Central University, Academia Sinica, Taiwan.

[2]Institute of Earth Sciences, Academia Sinica, Taiwan.

[3]School of GeoSciences, University of Edinburgh, EH9 3FE, UK.

[4]Scottish Universities Environmental Research Centre, G75 0QF, UK.

[5]Research Center for Environmental Changes, Academia Sinica, Taiwan.

[6]Department of Geosciences, National Taiwan University, Taiwan.

Corresponding author: Eh Tan (tan2@earth.sinica.edu.tw)

## Key Points

- The ZFT and ZHe ages (5.3 Ma and 2.6 Ma) are the oldest ages recorded in the middle Hsuehshan Range (mid-HR) in Taiwan.
- The exhumation rate in the mid-HR steadily increases from 0 to 3.4 km/Myr from 6.5 to 1 Ma and then increases at a slower rate.
- A steady increase in the exhumation rate indicates increasing topographic relief, which is likely caused by progressive crustal thickening.

## Abstract

The Taiwan orogenic belt has high precipitation and high exhumation rates (3-6 km/Myr), making it a natural laboratory for understanding how erosion, tectonics, and climate interact. Understanding how rock exhumation rates have evolved since the late Miocene is key to unraveling climate–tectonic interactions. In this study, we present 8 new zircon fission track (ZFT) and (U–Th)/He (ZHe) cooling ages (including 2 unreset ages) from 5 samples from

1,700 to over 3,300 m elevation around the highly incised Dajia River in the core of the Hsuehshan Range (termed the *mid-HR* in this study) in central Taiwan. Two of the ZFT and ZHe ages (5.3 Ma and 2.6 Ma) are the oldest ages recorded in this region. These ages suggest that the cooling rate of the mid-HR is lower than that of the Backbone Range and Yushan. With these and previously published cooling ages, we modeled the exhumation and cooling history using a 2-D thermal diffusion equation with time-varying erosion. The ZFT and ZHe ages are best explained by a steadily increasing exhumation rate up to 3.4+0.5/-0.3 km/Myr from 6.5 to 1 Ma. The exhumation rate in the last million years is not as well constrained but appears to have increased at a slower rate. Our findings differ from those of previous studies that propose that the exhumation rate increased rapidly in the last 1-2 Myr. We propose that the steady increase in the exhumation rate in the mid-HR indicates increasing topographic relief, which is likely caused by progressive crustal thickening.

## 1 Introduction

Taiwan is one of the youngest orogens on Earth, resulting from the convergence of the Eurasia continental margin and the Luzon volcanic arc (Ho, 1986; Teng, 1987, 1990) (Fig. 1). It is characterized by several high mountain ranges in the center of Taiwan. The island also receives high precipitation (121-361 cm annually) that is concentrated during the monsoon and typhoon seasons (Yu et al., 2006). The coincidence of high topographic relief and high precipitation means that the region currently experiences some of the highest exhumation rates (3-6 km/Myr) on Earth (Montgomery and Brandon, 2002; Dadson et al., 2003; Galewsky et al., 2006; Derrieux et al., 2014) as a result of rock uplift and erosion. The feedback between tectonic uplift, topography, climate, erosion and exhumation is complex and likely nonlinear. The uplift of the Tibetan Plateau and the Andes has nonlinear impacts on the climate and exhumation (Molnar et al., 1993; Braun et al., 2012; Carretier et al., 2013). In the Andes, for instance, the rising mountain range changed the regional precipitation, which in turn affected erosion and exhumation (Barnes et al., 2012; Carretier et al., 2013). Studies have found that exhumation increases nonlinearly after topography reaches the slope or elevation threshold. Similar effects might be present in Taiwan. To understand the process, it is crucial to constrain the history of the uplift/exhumation rates, paleotopography, and paleoclimate. As a first step, we present a detailed determination of the exhumation history, especially how it evolved and when its rate reached the present-day high values.

The long-term exhumation rate can be deduced from the rock cooling rates based on low-temperature thermochronometry (LTT). Cooling ages and fission track measurements have been modeled to determine the most likely cooling paths of the Taiwan orogenic belt (Liu, 1982; Liu et al., 2000; Willett et al., 2003; Fuller et al., 2006; Lee et al., 2006; Beyssac et al., 2007; Kirstein et al., 2010; Kirstein et al., 2013; Lee et al., 2015; Hsu et al., 2016; Chen et al., 2018; Chen et al., 2019; Huang et al., 2022; Lee et al., 2022).

With these data, two distinct tectonic implications are proposed. Willett et al. (2003) and Fuller et al. (2006) utilized numerical thermal models to simulate the cooling processes of the orogenic belt and suggested that the middle latitudes of Taiwan Island have reached a topographic steady state since 2.1-1.5 Ma (Fuller et al., 2006). This implication is consistent with morphological conclusions suggesting that the Taiwan mountain belt has reached a topographic steady state (Suppe, 1981; Barr and Dahlen, 1989; Deffontaines et al., 1994; Willett and Brandon, 2002; Stolar et al., 2007). Several thermochronological studies (Lee et al., 2006; Kirstein et al., 2010; Kirstein et al., 2013; Hsu et al., 2016; Chen et al., 2018) have found evidence of late rapid cooling and proposed the late rapid exhumation hypothesis, where the exhumation rate of Taiwan has rapidly increased in the last 1-2 Myr. This hypothesis was based on the exhumation history that was directly calculated from the cooling rate with the assumption of a constant geothermal gradient, but it was also based on an increased frequency of reset LTT ages (<6 Ma) in sediments younger than 1.9 Ma (Kirstein et al., 2010). As a result, it has been proposed that the uplift mechanism of the Taiwan Orogeny changed at approximately 1-2 Ma (Lee et al., 2006; Kirstein et al., 2010; Hsu et al., 2016; Chen et al., 2018). However, the geothermal gradient in the past is difficult to determine. Brown and Summerfield (1997) indicate that geothermal gradients likely vary significantly with time in tectonically active regions as hot, deep-buried rock is progressively advected to the surface. The late rapid exhumation proposal assumes a constant geothermal gradient and needs to be re-examined. To address the uncertainty in the geothermal gradient, a numerical thermal model is required (Braun et al., 2012; Coutand et al., 2014; McCallister et al., 2014; Fox et al., 2015; Wolff et al., 2020; Dai et al., 2021). Several tools that can obtain an exhumation history from thermochronological data have been developed and are widely used, including Pecube (Braun et al., 2012), Glide (Fox et al., 2014), and age2exhume (van der Beek and Schildgen, 2023). We opted to develop the thermochronological calculation within the thermal–mechanical model *flac* (Cundall, 1989; Tan et al., 2012). We use only the thermal model in this study and

plan to incorporate thermal–mechanical deformation with thermochronological modeling in a later study.

Taiwan is subdivided into a number of tectono-stratigraphic units from west to east, including the Coastal Plain, the Western Foothills, the Hsuehshan Range (HR), the Backbone Range (BR), the Longitudinal Valley and the Coastal Range. The HR is the second largest mountain range in Taiwan. It lies to the west of the BR. Both mountain ranges are oriented NNE–SSW and formed during the Taiwan Orogeny, which started at approximately 6.5 Ma (Suppe, 1984; Teng, 1992; Liu et al., 2001; Mouthereau et al., 2001; Lin et al., 2003; Kirstein et al., 2010). The earliest rocks that were exhumed during the formation of the BR have been eroded, and only sediment has been preserved in the Coastal Range (Dorsey & Lundberg, 1988). The oldest zircon fission-track (ZFT) ages from the core of the HR are 4.6 Ma (Lee et al., 2015). These ages are significantly younger than the onset of orogenesis, implying that the rocks that were exhumed earlier have been eroded away or have yet to be sampled. The HR has lower cooling and exhumation rates than the BR (Simoes et al., 2007; Derrieux et al., 2014); hence, it is more likely to preserve the record of the early stage of exhumation. Our study area is located in the core of the HR, and it is termed the *mid-HR* in this study.

Previously published thermochronological data from the mid-HR were predominantly collected along the Central Cross-Island Highway, which follows river valleys and cuts through several tectonic units (Tsao, 1996; Liu et al., 2001; Fuller et al., 2006; Lee et al., 2006; Lan, 2009; Liang, 2011; Lee et al., 2015). Most of these samples represent only limited elevation variation within each unit (1000−1500 m). A few samples from the highest elevations (Lee et al., 2015) have been analyzed with only ZFT. In this paper, we use ZFT and (U–Th)/He (ZHe) thermochronometry of high-elevation samples from the mid-HR to investigate the exhumation history and to test the late rapid exhumation model. The ZFT and ZHe age-elevation profiles are combined with published datasets (e.g., Tsao (1996); Liu et al. (2001); Fuller et al. (2006); Lee et al. (2006); Beyssac et al. (2007); Lan (2009); Liang (2011); Lee et al. (2015)) and a time-dependent 2-D thermal model with erosion to simulate the cooling history. We constrain the exhumation history of the HR and discuss the implications for exhumation.

## 2 Geological background

Taiwan is located on the boundary between the Philippine Sea Plate and the Eurasia Plate (Fig. 1). The Philippine Sea Plate is moving at ~82 mm/yr in a NW direction with respect to the Eurasian plate (Yu et al., 1997). The HR was a Paleogene half-graben filled with Eocene-

to-Oligocene sediments, which were metamorphosed during the Taiwan Orogeny (Teng, 1992, 2007). The strata in the HR have undergone deep burial (~10 km) and moderate greenschist-facies metamorphism (300−450°C) (Chen and Wang, 1995; Fuller et al., 2006; Beyssac et al., 2007; Chen et al., 2018). The foreland sandstone consists of clasts sourced from the mid-HR. Chen et al. (2019) analyzed sandstones to constrain when the metamorphic rocks were exposed on the surface and found that the onset of exhumation of the mid-HR likely occurred earlier than 4.3 Ma, which is consistent with the oldest reset ZFT age of 4.6 Ma in this region (Lee et al., 2015). ZFT ages in the central core of the mid-HR are all reset and younger than 6.5 Ma, which indicates that they were cooled during the Taiwan Orogeny. In contrast, ZFT ages from the eastern and western flanks are older (14.6-100 Ma), indicating that they have not been heated above 300°C in the last 14 Myr (Fig. 1). This finding indicates that the central core has experienced the highest exhumation (Fuller et al., 2006; Beyssac et al., 2007). In addition to zircon, apatite is another common mineral for LTT. Unfortunately, apatite grains are rarely contained in the source rock in the mid-HR. Therefore, their ages are not included in this study.

No cooling rate has been reported for the mid-HR. In the northern HR, the cooling rate was negligible between 6 and 2.5 Ma, increased to 120°C/Myr between 2.5 and 1.6 Ma and then became 90°C/Myr since 1.6 Ma (Chen et al., 2018). Inverse thermal modeling in the northern BR (to the east of the mid-HR) indicates that the cooling rate was 5-21°C/Myr before 2.5 Ma, increased significantly to 75-85°C/Myr between 2.5 and 0.5 Ma and increased further to 460-530°C/Myr in the last 0.5 Myr (Hsu et al., 2016). The cooling history from the adjacent regions suggests that the mid-HR also experienced late rapid cooling in the last 2 Myr.

The present-day geothermal gradient of the HR is likely high but spatially varying. The present-day surface heat flow in the HR is derived from thermal wells (Lee and Cheng, 1986; Wu et al., 2013) and silica geothermometry (Liu et al., 2015) is approximately 50-300 $mW/m^2$, which corresponds to a geothermal gradient of 30-90°C/km near the surface. Within the top 10 km, the average geothermal gradient, which is inferred from the Curie depth, is approximately 50°C/km (Hsieh et al., 2014).

The uplift mechanism of the HR has been proposed through three primary concepts: basal accretion and underplating at the decollement (Chapple, 1978; Suppe, 1981; Davis et al., 1983; Barr and Dahlen, 1989; Simoes et al., 2007), the fault-bounded pop-up structure (Clark et al., 1993; Lee et al., 1997), and subvertical elongation (Clark et al., 1993; Tillman and Byrne, 1995). The deformation in the mid-HR is mainly due to ductile folding rather than brittle faulting (Liu et al., 2009). The folds are widely distributed and have wavelengths of tens to

several thousands of meters (Liu and Kao, 2011). Previous studies have indicated the penetrative coaxial strain history and the subvertical elongation of the HR (Clark et al., 1993; Tillman and Byrne, 1995) Additionally, Kidder et al. (2012) suggest an axial strain of 0.3 during deformation at the Kuangmingchiao Anticlinorium (Kmc) (also known as the Dachein Anticline) located at approximately 121.1°E in Fig. 1. The coaxial deformation in the mid-HR makes the Kmc a suitable target for our study.

We collected samples along the A-A' profile (Fig. 1), which runs parallel to the Kmc in a NE–SW direction. This profile cuts through the Dajia River valley (Fig. 1) and extends from the riverbed (1000 m elevation) to the mountain peak (3300 m elevation). The profile is 7 km long and has a height difference of 2.3 km. We collected three coarse-grained meta-sandstone samples from the Eocene Tachien Formation along the A-A' profile and another two samples from the Paileng Formation in the northwestern region (Fig. 1).

## 3 Thermochronology

Zircons were separated and picked under a binocular microscope from the 75-350 μm fraction of crushed samples. ZFT dating followed the procedures of Liu et al. (2000) and used the external detector method for sample processing and age calculations. The zeta (ζ) factor (Hurford and Green, 1983) for the standard Fish Canyon Tuff with standard glass NBS-610 was determined to be 30 ± 2 Ma (1σ).

The ZHe analysis was conducted in the Noble Gas Laboratory at the Scottish Universities Environmental Research Centre. Two to four replicate grains were analyzed for ZHe ages. Each grain was hand-picked, and its dimensions were measured before being loaded into Pt tubes. We followed the procedures of Foeken et al. (2006) for He extraction/analysis and Dobson et al. (2008) for U and Th measurements. The analytical uncertainty in each grain age is 3-5%, mostly due to the uncertainty in the $^{4}$He standard and U and Th spike concentrations (Maino et al., 2019). Correction for He recoil loss was made with established procedures (Hourigan et al., 2005). We assume the uncertainty in grain ages after the correction to be 5%. Age calculations were made following Meesters and Dunai (2005). The uncertainty of the mean age is the standard deviation of the grain ages. If the standard deviation is less than 5% of the mean age, we assume the uncertainty to be 5%.

The ZFT and ZHe ages of all samples are listed in Table 1. The peak, pooled, and central ZFT ages were calculated and reported for each sample. If the measured thermochronometric age is younger than the onset of the Taiwan Orogeny (6.5 Ma), the grain

188 is considered to be reset. In the following discussion, central ages are used for reset samples.
189 Two ZFT ages (from samples SP01 and ML02) from the Oligocene Paileng Formation in the
190 northwest region are older than 6.5 Ma. These grains have not been reset by the Taiwan
191 Orogeny and are not included in later discussion. The oldest reset ZFT age (5.3 ± 0.5 Ma) is
192 recorded by sample BG02 from the peak of Mt. Baigu (3,189 m), while the youngest age, 3.8
193 ± 0.4 Ma, is recorded by sample DG01 from an elevation of 1,711 m. ZHe ages from these
194 samples range from 2.62 ± 0.13 Ma to 1.94 ± 0.10 Ma (Fig. 2). These new ages from high-
195 elevation samples are older than previously published ZFT cooling ages (Fig. 1) and provide
196 important new constraints on the early exhumation history of the region.

197 A recent development indicates that the ZHe closure temperature could be significantly
198 lower than that calculated by Brandon (2007) due to α-dose damage (Gérard et al., 2022). The
199 work of Gérard et al. (2022) is important for the interpretation of LTT ages, where ZHe, apatite
200 fission track (AFT) and apatite helium ages overlap, specifically where the ZHe ages are
201 younger than the AFT ages. However, there is no evidence of overlapping LTT ages in this
202 region. An AFT age of 0.702 ± 0.28 Ma (Lock, 2007) cited by Chen et al. (2019) is in the river
203 valley of our AER profile. The sample was collected from an elevation of 1286 m. The ZHe
204 ages at a similar location are 1.36 ± 0.10-1.51 ± 0.02 Ma (Beyssac et al., 2007), with elevations
205 of 1039-1487 m. This finding indicates that the effect of α-dose damage is not important here.

206 The age-elevation relationships (AERs) and previously published data (Table 2) of the
207 A-A' profile are plotted in Fig. 3. A positive correlation between the ZFT and ZHe ages and
208 elevation is clear. We can estimate the apparent exhumation rate from the AERs using two
209 different approaches. First, the slopes of the AERs indicate that the apparent exhumation rates
210 were ~1.4 km/Myr from 5 to 2.5 Ma and ~1.9 km/Myr from 2.5 to 1.5 Ma, showing a moderate
211 increase in the exhumation rate over time. Second, the apparent exhumation rate can be derived
212 from the apparent cooling rate, which is derived from the difference between the ZHe and ZFT
213 ages. Assuming a constant ZFT closure temperature of 240°C (Hurford, 1986) and a ZHe
214 closure temperature of 180°C (Beyssac et al., 2007), the apparent cooling rates can be estimated
215 as ~32°C/Myr at 5.5-2.5 Ma from a high-elevation AER (yellow line above 3000 m in Fig. 3),
216 ~39°C/Myr at 3-1.5 Ma from a low-elevation AER (yellow line below 1000 m in Fig. 3), and
217 ~108°C/Myr from 1.5 Ma to the present day from a low-elevation ZHe (yellow line at
218 approximately 2000 m in Fig. 3). The evolution of the apparent cooling rate is consistent with
219 the previously reported late rapid cooling after ~2 Ma in the HR and BR (Lee et al., 2006;
220 Kirstein et al., 2010; Kirstein et al., 2013; Hsu et al., 2016; Chen et al., 2018; Chen et al., 2019).

The apparent exhumation rate can be estimated from the age vs. elevation of the same thermochronometer by assuming an unchanged distance between the surface and closure isotherm (i.e., a constant average geothermal gradient). The result (blue line in Fig. 3) is that the apparent exhumation rate was 1.4 km/Myr ($r^2 = 0.71$) during 5-3 Ma and 1.9 km/Myr ($r^2 = 0.95$) during 3-1.5 Ma. The apparent exhumation rate during 1.5-0 Ma can be estimated from the apparent cooling rate by assuming a conventional geothermal gradient. Using 25°C/km, the exhumation rate is ~4.3 km/Myr. This again shows a moderate increase during 5-1.5 Ma followed by a rapid increase in the last ~2 Myr, which seems to be consistent with the proposal of late rapid exhumation (Lee et al., 2006; Kirstein et al., 2010; Kirstein et al., 2013; Hsu et al., 2016; Chen et al., 2018; Chen et al., 2019). The ZHe samples at low elevations have very similar ages, indicating a high erosion rate around 1.5 Ma.

However, the estimates of apparent cooling and exhumation are based on the assumption of constant closure temperatures and geothermal gradients. It is well known that mineral closure temperatures increase when the cooling rate increases (Dodson, 1973, 1979). For example, the closure temperatures of ZFT and ZHe are 232°C and 183°C, respectively, when the cooling rate is 10°C/Myr, and they become 256°C and 207°C, respectively, when the cooling rate is 100°C/Myr (Brandon et al., 1998; Reiners et al., 2004). Additionally, Taiwan is not in a thermal steady state, and its geothermal gradient definitely changes both spatially and temporally. For such a young orogen with high erosion, heat cannot diffuse out sufficiently, leading to a temporal increase in the near-surface geothermal gradient (Brown and Summerfield, 1997). Consequently, the hypothesis of late rapid cooling and exhumation is subject to significant uncertainty. In the following section, we eliminate the assumptions of the constant closure temperature and geothermal gradient by applying a time-dependent thermal model. This model enables us to constrain the evolution of the exhumation rate during the Taiwan Orogeny.

## 4 Time-dependent thermal models

We modeled the thermal evolution and thermochronometer cooling ages within the A-A' profile with a time-dependent thermal diffusion equation on a 2-D Lagrangian grid. We use *Geoflac for thermochronology* (Shyu et al., 2023), which is based on the *Fast Lagrangian Analysis of Continua (FLAC*) algorithm (Cundall, 1989; Tan et al., 2012) and is integrated with thermochronology. The equation of thermal diffusion is solved explicitly as:

252 $$\frac{\partial \mathrm{T}}{\partial \mathrm{t}} + v_{\mathrm{z}} \frac{\partial \mathrm{T}}{\partial \mathrm{z}} = \frac{\mathrm{k}}{\rho \mathrm{C_p}} \frac{\partial^2 \mathrm{T}}{\partial \mathrm{z}^2}$$

253 where T is the temperature (°C), t is time (s), k is the thermal conductivity (3.3 W/m/K),
254 ρ is the density (2800 kg/m$^3$), $C_p$ is the specific heat (1000 J/kg/K), and $v_z$ is the imposed uplift
255 rate (m/s). The top surface has a fixed temperature of 10°C. The other boundaries are thermally
256 insulating. The top surface is eroded and has a prescribed erosion rate to simulate exhumation.

257 The ZFT and ZHe closure temperatures are cooling-rate dependent (Dodson, 1973,
258 1979), as calculated by CLOSURE (Brandon et al., 1998; Brandon, 2007). The time of closure
259 is recorded as the closure age of the thermochronometer.

260 The model domain consists of a 7-km wide and 50-km thick block. The grid spacing is
261 200 m. The Kmc profile has a 2.4 km elevation change in a 7 km horizontal distance. We
262 assume that there is no lateral motion within the domain, and we discuss the validity of the
263 assumption in a later section. With no lateral motion within the profile, the erosion rate at the
264 surface is identical to the exhumation rate of buried material. We further assume that there is
265 no differential uplift within the profile since the profile is parallel to the major tectonic lineation
266 and does not cut across the major tectonic structure. As a result, the height difference within
267 the profile is produced completely by differential erosion (Fig. 4).

268 The geothermal gradient of the mid-HR at maximum burial was estimated by Raman
269 spectroscopy of carbonaceous material (RSCM) to be 25-30°C/km (Beyssac et al., 2007). It is
270 unclear when the temperature gradient reported by RSCM was recorded. The maximum burial
271 temperature is reported as 450°C, which is within the domain of high-grade greenschist facies.
272 However, only low-greenschist facies (~300°C) has been found in the sediments from the HR
273 (Yeh, 2017; Chen et al., 2019). Our samples do not show evidence of greenschist-facies
274 metamorphism, and it is very unlikely that our samples were heated above 300°C. In addition,
275 if temperatures in the region of 450°C were attained during the Taiwan Orogeny, zircons with
276 reset ZFTs, whose closure temperature is ~240°C, should have been exposed much earlier than
277 1 Ma (Wu, 2018). Therefore, we suspect that the high burial temperature recorded by the
278 RSCM is likely a prior heating event experienced before the Taiwan Orogeny initiated. With
279 this uncertainty in mind, we consider the initial geothermal gradient as a model parameter.

280 The HR was initially a sedimentary half-graben. We assume that the initial topography
281 and isotherms were flat. However, adopting a uniform gradient over the whole depth results in
282 exceedingly high temperatures and overcooling in the lower half of the model. The geothermal

283 gradient should decrease with depth. We use a half-space cooling model for the initial
284 temperature and vary its half-space age parameter. Although the half-space cooling model is
285 valid only for oceanic lithosphere, as it ignores radiogenic heat production and the past thermal
286 history of the continental lithosphere, it gives a reasonable approximation for the near-surface
287 temperature profile. The mantle temperature is 1300°C, and the surface temperature is 10°C.
288 This half-space age parameter is unrelated to the cooling age of thermochronometers but only
289 a model parameter for the initial temperature. To avoid confusion, we list the corresponding
290 initial surface geothermal gradient ($G_t$) within the top 200 m of the half-space cooling model
291 as the model parameter output.

292 The exhumation is driven by surface erosion. The area that later became Taiwan was a
293 submarine sedimentary environment (Teng, 1990, 1992). Therefore, we assume that the
294 erosion rate is 0 km/Myr before the orogeny. We note that the absolute elevation of the surface
295 has no impact on our thermal model. The model surface has no height difference at the
296 beginning, but its elevation could be subzero. At the early stage of the collision, the area may
297 still be submarine and experience submarine erosion. At later stages, the area rises above sea
298 level and experiences subaerial erosion. Both are included in the erosion in our models. The
299 erosion rate is 1 km/Myr in the young collision zone in southern Taiwan and increases to ≥4
300 km/Myr in the mature orogen in central Taiwan (Fellin et al., 2017). This suggests that the
301 erosion rate in Taiwan has increased as the orogen matured. Additionally, the river valley has
302 a higher erosion rate than the mountain. Hence, the surface erosion rate in our model is
303 prescribed as a function of both space and time. It can be written as

304 $$\text{erosion rate} = \mathrm{R(t)}\left(1 + \Delta\mathrm{R}\cos\left(\frac{x}{L}\pi\right)\right)$$

305 where R(t) is the time-dependent spatially averaged erosion rate, ΔR is the amplitude
306 of differential erosion between the valley and hill, and *L* is the distance between the valley and
307 hill (7 km). The prescribed high-erosion region becomes the valley ($x$=0), and the low-erosion
308 region becomes the peak ($x$=$L$). The temporal average of R(t) is reported as the temporal
309 average erosion rate ($R_{avg}$). We assume that the surface height difference increases with time
310 and that the rate of increase is proportional to the erosion rate R(t). The proportional constant
311 ΔR is chosen so that the difference in elevation is 2.4 km (shaded area in Fig. 5a-b) at the end
312 of the simulation.

313 We consider two scenarios for the evolution of R(t). The first scenario has a constant
314 erosion rate during the simulation (Fig. 5a). The scenario can be described by two parameters:

the temporal average erosion rate, $R_{avg}$, and the model duration, $t_f$ (6 or 7 Myr), which is the duration since the onset of exhumation (Liu et al., 2001). We found that the misfits of these constant models are large, so we have to resort to a more complicated scenario. In the second scenario, the erosion rate is 0 before the orogeny, gradually increases as the orogeny progresses, and may further increase, saturate, or decrease at the late stage of the orogeny. Specifically, we consider the time-varying scenario in two stages (Fig. 5b). At each stage, R(t) is linear. This scenario has four parameters – the model duration ($t_f$), R(t) at the end of the second stage ($R_f$), duration of the first stage ($t_m$), and R(t)/$R_f$ at $t_m$ ($r_m$). The temporal average erosion rate $R_{avg}$ is affected by these parameters.

We vary the initial geothermal gradient ($G_t$), erosion rate parameters ($R_{avg}$, $r_m$, and $t_m$), and model duration ($t_f$) (Table 3). Although the cooling is controlled by erosion and is not affected by elevation, to match the topography of the A-A' profile (whose average elevation is 2.2 km high) at the end of the model time, a constant uplift rate ($v_z$) is applied to each model and is equal to $R_{avg}$ + 0.367 km/Myr for $t_f$ = 6 Myr or $R_{avg}$ + 0.315 km/Myr for $t_f$ = 7 Myr.

## 5 Results

The model surface is flat at an elevation of 0 km (i.e., no height difference) at the beginning. The surface height difference increases gradually over time because of differential erosion. As erosion removes material from the surface, the uplifting rock cools. Exhumation first occurs in the valley and then at the mountain summit. After a model time of $t_f$, every model reaches a height difference of 2.4 km. The closure ages and their elevations at the surface are then compared to the laboratory AERs in Fig. 3.

We evaluate the model AER results by calculating the difference between the model AER and the laboratory results at the same elevation, weighted by the sample standard deviation. The misfit (s) of the model result is defined as

$$s = \frac{\sum_{i=1}^{m}\left(\frac{(zhe_{Num} - zhe_i)^2}{\sigma_i^2}\right)}{2m} + \frac{\sum_{j=1}^{n}\left(\frac{\left(zft_{Num} - zft_j\right)^2}{\sigma_j^2}\right)}{2n}$$

where $m$ is the number of ZHe ages, $n$ is the number of ZFT ages, $zhe_{Num}$ is the modeled ZHe age, $zft_{Num}$ is the modeled ZFT age, $zhe_i$ is the $i$-th ZHe laboratory age, $zft_j$ is the $j$-th ZFT laboratory age, $\sigma_i$ is the standard deviation of the $i$-th laboratory ZHe age, and $\sigma_j$ is the standard deviation of the $j$-th laboratory ZFT age.

We plot the model misfits with respect to the initial thermal gradient $G_t$ and the time-averaged erosion rate $R_{avg}$ (Fig. 6). If the reset ZHe/ZFT is not exhumed to the surface or only partially exhumed, the model misfit is colored dark or light gray, respectively, which occurs when $G_t$ and $R_{avg}$ are both low. Within each series, the trade-off between $G_t$ and $R_{avg}$ is clear. A model with a high $R_{avg}$ and low $G_t$ has a similar misfit to a model with a low $R_{avg}$ and high $G_t$.

This scenario is tested by varying $r_m$, $t_m$, and $t_f$ in a total of 124 series of models (Fig. 7a, Table 3). We have considered all reasonable variation patterns of the erosion history. For each series, 572 models with varying $R_{avg}$ and $G_t$ values are explored. The lowest-misfit models within each of the 124 series are shown in Fig. 7. We classify 124 series of models into 4 types based on how the erosion rate changes with time and label the representative models (Models A-D) in each type (Fig. 7b-c, Table 3): constant (Model A), near-steady increase (Model B), early rapid increase (Model C), and late rapid increase (Model D).

### 5.1 Representative models of four types

From the representative models of these four types, the models with near-steady increases (Model B) and early rapid increases (Model C) share the lowest and similar misfits. These two models have similar $G_t$ and $R_{avg}$ values. Here, we describe Model B (Series 6 in Table 3) in detail. This is one of the best-fit models (misfit = 1.428), where the erosion rate increases rapidly from 0 to 1.49 km/Myr from 6 to 5 Ma and then increases less rapidly to 3.73 km/Myr at the present day (Line B in Fig. 7b). The erosion rate reaches 40% of the present-day value at 5 Ma. The model has values of $R_{avg}$ = 2.3 km/Myr, $R_f$ = 3.73 km/Myr, and $G_t$ = 17.47°C/km. The material exposed in the valley experiences a rapid change in the local geothermal gradient during exhumation. The local geothermal gradient is ~17°C/km at a depth of ~15 km at 6 Ma, ~19°C/km at a depth of ~10 km at 3 Ma, and ~71°C/km at the surface at the present day. The average geothermal gradient is ~32°C/km within the top 10 km depth at the present day (black line in Fig. 8d). The final surface geothermal gradient is nearly four times higher than the initial value. The comparison of the model erosion and cooling rate (red lines in Fig. 7b and 7c) clearly shows that the variations in these rates are not correlated. There is an ~4 Myr time lag between the onset of the distinct increase in the erosion and cooling rates in the model. For a young orogenic belt, such as Taiwan, this time lag is a significant portion of the orogen history, which needs to be taken into account when using thermochronometers to provide insight into orogen evolution. Model C (Series 120 in Table 3) also has a small but

slightly higher misfit of 1.532 than Model B. The erosion rate gently decreases in the last 1 Myr (Line C in Fig. 7b). The AERs of this model (green lines in Fig. 7d) are very similar to those of Model B, demonstrating the nonuniqueness of thermal modeling.

Model D (Series 41 in Table 3), with a late rapid increase in the erosion rate, has the highest misfit of 62.44 among the four representative models. In this model, erosion slowly increases in the first 4 Myr and rapidly increases in the last 2 Myr (Line D in Fig. 7b). The final erosion rate is 3.16 km/Myr. The AERs of this model (blue lines in Fig. 7d) have the shallowest slope among the representative models. However, the age at a low elevation is too young. Indeed, all late-rapid-increase models have large misfits. This is contradictory to the late rapid erosion proposed by previous studies in the HR (Hsu et al., 2016; Chen et al., 2018).

Model A (Series 1 in Table 3) has a medium misfit of 5.042. The erosion rate is constant from 6 Ma to the present day (Line A in Fig. 7b). The AERs of Model A (red lines in Fig. 7d) have steep slopes and small age differences between the ZHe and ZFT AERs. The fit for the ZHe is satisfactory. However, the ZFT AER is too young and does not match the laboratory results.

### 5.2 Ensemble average of low-misfit models

Several models share similar low misfits, demonstrating the nonuniqueness of forward modeling. We take the ensemble of the top 17 best-fit models (misfits ≤ 1.60; Series 6, 7, 17, 18, 33, 64, 74, 85, 86, 99, 109, 110, and 119-123) to calculate the average erosion rate of the mid-HR (black line in Fig. 7b) and use this ensemble average as our best estimate. Error bars represent the range of 17 best-fit models at each time. The ensemble average exhumation rate is 2.2+0.5/-0.4 km/Myr. The initial average geothermal gradient is 17.1+3.4/-2.6°C/km. Erosion increases steadily from 0 to 3.4+0.5/-0.3 km/Myr from 7 Ma to 1 Ma. The linear increase is well constrained. After 1 Ma, the slope of the erosion rate is reduced with larger uncertainty. We have less confidence in the slowing of the rate increase.

We also calculate the ensemble average of the cooling rates of the top 17 best-fit models (black line in Fig. 7c). The cooling rate increases monotonically and nonlinearly to 121+4.4/-3.6°C/Myr from 7 Ma to 0.5 Ma, followed by a slower increase in the cooling rate with greater uncertainty at the present day. We find that all cooling histories of the best-fit models (Fig. 7c) have a similar trend among the 124 model series, regardless of the erosion history. The cooling rates are low (<30°C/Myr) from 7 to 3 Ma. After 2 Ma, the cooling rates start increasing significantly and reach approximately 100°C/Myr at 1 Ma. The onset of rapid cooling usually

occurs at approximately 2 Ma, despite the variability in the erosion history. When the material is exhumed close to the surface, where the geothermal gradient is high due to earlier erosion, the rock experiences rapid cooling. This is why all thermochronological records in the HR or BR show a rapid increase in the cooling rate from 2 Ma (Lee et al., 2006; Kirstein et al., 2010; Hsu et al., 2016; Chen et al., 2018). The rapid increase in the cooling rate does not necessarily imply an increase in the exhumation/erosion rate, as noted by Mancktelow and Grasemann (1997).

# 6 Discussion

## 6.1 Comparisons to geological observations

Notably, the erosion rates from the model are consistently higher than the apparent rates suggested by the AER. This is because the apparent erosion rate is calculated based on the assumption that the closure depth remains constant over time. However, the geothermal gradient in the HR increases with time. As a result, the closure depth is shallower at the present day than in the past. For example, the ZFT closure depth in Model B migrates upward by ~2 km from 5 Ma to 2.5 Ma (red circles in Fig. 8). This upward migration is not considered when calculating the apparent erosion rate. Therefore, it underestimates the true erosion rate. In Model B, the height difference is 2.4 km, while the total exhumation is ~5 km (depth of 13 to 7.9 km) in this same time period (brown diamonds in Fig. 8d). This results in an apparent erosion rate of ~1 km/Myr and a true erosion rate of ~2 km/Myr. This difference between apparent and true erosion rates can be estimated only via a forward thermal model.

There is evidence of a 1 km/Myr submarine erosion rate south of Taiwan (Das et al., 2021). The study area of Das et al. (2021) has a > 3 km height difference over the nearby sea floor. This indicates that the region is already uplifting, which suggests that this 1 km/Myr erosion rate does not represent the erosion rate at the onset of collision. The erosion rates in Models B and C at 5-6 Ma are ~1 km/Myr. These results suggest that it took approximately 1 million years after the onset of collision for the erosion rate to reach 1 km/Myr.

We found that the cooling rates in the later stage (< 2 Ma) are consistently much higher than those in the early stage (> 4 Ma) in our models. The ensemble average of the cooling history (black line in Fig. 7c) shows an extremely low cooling rate (<10°C/Myr) from 7 to 4 Ma and a low cooling rate (10-20°C/Myr) from 4 to 3 Ma. Then, the cooling rate increases rapidly from 20°C/Myr at 3 Ma to over 130°C/Myr at the present day. This cooling history is generally consistent with multi-thermochronometric data in the northern HR (Chen et al., 2018).

Chen et al. (2018) studied the cooling history of a nappe from the northern HR and found that the sample was in a nearly isothermal state until 2.5 Ma, after which the cooling rate increased to 120°C/Myr during 2.5-1.5 Ma and slightly decreased to 90°C/Myr from 1.5 Ma to the present day (green line in Fig. 7c).

Model B not only fits the AERs but also satisfies other geological constraints. Model B has an almost linear increase in the maximum burial temperature of exposed samples over time. The exposed maximum burial temperature increases from 100°C at 3 Ma to 210°C at 1 Ma and finally to 270°C at the present day (black line in Fig. 9). Model B predicts that very low-grade metamorphic rocks (maximum burial temperature of 200°C) were exhumed to the surface at ~1 Ma, which is supported by petrographic analyses of the sandstone in the Dajia River basin (Yeh, 2017; Chen et al., 2019).

The youngest ages are always exposed first at the valley. The reset ZFT in Model B is first exposed at 0.8 Ma with an age of 4.6 Ma and then gradually become younger, with an age of 2.6 Ma at the present day (dashed blue line in Fig. 9). The late exposure of reset ZFT ages is consistent with the observation that reset detrital ZFT ages can be found only within young strata (< 1 Ma) in the Dajia River basin (Wu, 2018). In addition, the reset ZHe in Model B is first exposed at 1.6 Ma with an age of 4 Ma and then gradually become younger, with an age of 1.5 Ma at the present day (solid blue line in Fig. 9). Model B predicts that a reset detrital ZHe value would appear only in strata younger than 1.5 Ma. This prediction awaits future verification.

Our thermal simulations can predict the geothermal structures. We take the thermal gradient of the top element layer of the model to calculate the surface geothermal gradient and heat flow. The average surface geothermal gradients and heat flows of the four representative models are as follows: Model A: 39°C/km (128 mW/m$^2$); Model B: 43°C/km (143 mW/m$^2$); Model C: 41°C/km (135 mW/m$^2$); and Model D: 65°C/km (213 mW/m$^2$). The model with a late rapid increase in the erosion rate (Model D) has the highest heat flow, while the model with a constant erosion rate (Model A) has the lowest heat flow. The heat flow of the best-fit model (143 mW/m$^2$) is higher than the observed regional heat flow (100-120 mW/m$^2$, Liu et al. (2015)). Then, the average thermal gradient from the top 10 km of the best-fit model (Model B) is 32°C/km, which is lower than the observed regional thermal gradient, as determined by the depth of the Curie point (~50°C/km, Hsieh et al. (2014)). Unfortunately, we cannot reconcile this conflict. Further research is needed.

### 6.2 Comparison to the model of Simoes et al. (2007)

Simoes et al. (2007) also modeled the thermokinematic evolution of the HR. Here, we compare our model results with theirs. Their exhumation rate is 4.2 km/Myr, starting at 4 Ma, with a total exhumation of 16.8 km. Our ensemble average has a lower average erosion rate (2.2+0.5/-0.4 km/Myr), earlier initiation (6-7 Ma), and lower total exhumation (13.2-15.4 km). We attribute the discrepancy to the inclusion of newly reported ZHe and ZFT ages from high elevations and the exclusion of the RSCM temperature (Beyssac et al., 2007). Most of the reset ages used in Simoes et al. (2007) were sampled from elevations of 1000-2000 m in the HR. Our high-elevation thermochronological ages are older than the ages used in Simoes et al. (2007), which are less than ~4 Ma (Liu et al., 2001). The older ages push the initiation time of HR exhumation earlier. The lengthened history of the HR decreases the average erosion rate. In addition, the RSCM temperature (Beyssac et al., 2007) in the HR is high (~450°C), which suggests a deep burial depth and high exhumation. If the RSCM temperature is included for fitting, we would need to either increase the initial geothermal gradient $G_t$ or the erosion rate. Both changes would reduce the ZHe and ZFT ages, as well as the age difference between them, which would lead to poorer model fits. As discussed in Section 4, we argue that the reported RSCM temperature was likely not acquired during the Taiwan Orogeny but during an earlier heating event. Therefore, the RSCM temperature is excluded from our data.

### 6.3 Onset of exhumation

We compared two pairs of model series to distinguish the onset of exhumation. The variations in the misfits are opposite between the models. In the pair of models with constant erosion, the misfit of the model with $t_f$ = 7 Myr (Series 2 in Table 3) is larger than that of the model with $t_f$ = 6 Myr (Series 1). In the pair with linear-increasing erosion, the misfit of the model with $t_f$ = 7 Myr (Series 94) is smaller than that of the model with $t_f$ = 6 Myr (Series 31). Among the best-fit models (misfit ≤1.60), 5 models (Series 6, 7, 17, 18, and 33 in Table 3) have $t_f$ = 6 Myr, and 12 models (Series 64, 74, 85, 86, 99, 109, 110, and 119-123) have $t_f$ = 7 Myr. Therefore, our results cannot distinguish the onset of exhumation in the mid-HR between 6 or 7 Myr.

### 6.4 Implications for Taiwan tectonics

Our results suggest steadily increasing exhumation in the mid-HR. Montgomery and Brandon (2002) reported that the erosion rate increases with the topographic relief of the mountain range. The long-term increase in the erosion rate implies that the large-scale E–W

topographic relief in the mid-HR progressively increased during the Taiwan Orogeny. In the last 1 Myr, the erosion rate appears to increase at a slower rate. Fuller et al. (2006) shows that the erosion rate becomes nearly constant once the mountain belt reaches the topographic steady state. This suggests that the mid-HR may be approaching a topographic steady state.

The steady increase in the exhumation rate likely resulted from progressively thickened crust. The thickening is recorded by steeply dipping penetrative cleavage (Clark et al., 1993; Tillman and Byrne, 1995). Crustal thickening elevates the topography and increases topographic relief, which in turn increases erosion. We further hypothesize that the progressive crustal thickening is due to constant horizontal shortening from the collision between the Eurasian continental margin and the Luzon arc. If this is true, it has strong implications for the orogenic process in Taiwan.

Our newly acquired ZHe ages at high elevations (above 3000 m) in the mid-HR region are approximately twice as old as those in the BR (Lee et al., 2022) and Yushan (Hsu et al., 2016), indicating a significantly lower cooling rate in the mid-HR than in the BR and Yushan. The lower cooling rate of the mid-HR could be attributed to either a lower erosion rate or a deeper closure depth. The long exhumation history of the BR, dating back to 12 Ma (Lo and Yui, 1996; Chen et al., 2019), implies that the geothermal gradient of the BR is higher than that of the mid-HR, resulting in a shallower closure depth and higher cooling rate. However, the comparison of exhumation rates in the BR requires further numerical investigation. For the Yushan region, the similar (Lee et al., 2015) or shorter (Liu et al., 2001) duration of the exhumation history suggests a similar or deeper closure depth but definitely a higher exhumation rate, resulting in a considerably higher cooling rate in the Yushan region. Nonetheless, a further numerical simulation for the Yushan region is still needed to sort out the exhumation histories among the ranges during the Taiwan Orogeny.

### 6.5 Constraints on erosion rates before 5 Ma and after 1.5 Ma

Our ensemble average has a smaller uncertainty between 1.5 and 5 Ma, where cooling ages are available, and has larger uncertainty before 5 Ma and after 1.5 Ma. It is natural to question how well constrained the erosion rates are before 5 Ma and after 1.5 Ma. To address this question, we compare two models, Models A and A' (Series 1 and 71* in Table 3), with very similar $G_t$ values and erosion histories, except for the erosion rate at 6-7 Ma, to gauge the effect of early erosion. Model A has a constant erosion rate, starting from 6 Ma. Model A' has an earlier onset of erosion at 7 Ma. Its erosion rate starts from 0 and reaches a value similar to

536 that of Model A at 6 Ma (Fig. 7b). Model A' has a 2% lower $R_{avg}$ and $G_t$ but higher total
537 exhumation than Model A. It has slightly younger ZFT ages (pink line in Fig. 7d) and a higher
538 misfit than Model A. The earlier onset of erosion of Model A' increases the near-surface
539 geothermal gradient and results in a younger cooling age. This indicates that erosion before 5
540 Ma would change the later temperature and affect the cooling ages. Similarly, erosion after 1
541 Ma changes the total amount of exhumation. Higher total exhumation would result in younger
542 cooling ages. Therefore, we conclude that the erosion rates before 5 Ma and after 1.5 Ma are
543 constrained by the integrated total exhumation.

544 **6.6 Relative motion in the profile plane**

545 In our thermal models, we assume that the material is uplifted at a uniform velocity for
546 simplicity (Fig. 4). This assumption might not be consistent with the regional tectonics, where
547 relative motion within the profile plane might exist. The relative motion can be decomposed
548 into three components: displacement in the plane, displacement out of the plane, and vertical
549 stretching. The A-A’ profile is parallel to the major tectonic lineation, which suggests that
550 displacement in the plane is insignificant. We discuss the importance of the other two
551 components individually, as well as their effects on our results.

552 Some studies (Suppe, 1981; Carena et al., 2002; Huang et al., 2015) indicate that there
553 is a detachment beneath the HR (Hung et al., 1999; Shyu and Sieh, 2005; Yue et al., 2005).
554 Materials pass through the profile plane below the detachment and may be underplated. The
555 thermal effect of this deformation is extra cooling at the detachment. This suggests that the
556 erosion rate in the mid-HR might be underestimated in our model. However, this effect should
557 be small. The major deformation mechanism in the mid-HR is folding with the coaxial strain
558 (Liu and Kao, 2011) rather than shearing, which indicates that the surface strata in the mid-HR
559 are not directly disturbed by the deformation at the detachment. The former detachment or
560 underplated material is still buried and yet to be exhumed.

561 Subvertical elongation does occur in the HR (Clark et al., 1993; Tillman and Byrne,
562 1995). The shortening strain is approximately 0.3 in the HR (Kidder et al., 2012). Conversely,
563 the vertical stretching is approximately 1/(1-0.3)=1.4 times the original thickness. Stretching
564 affects the thermal structure by homogenously decreasing the geothermal gradient. Therefore,
565 the initial geothermal gradient of the best-fit model might be underestimated.

### 6.7 Erosion and climate feedback

Erosional processes can shape the topographic relief of the orogenic belt. The regionally high altitude would impact the local climate, and the precipitation variability could change erosional exhumation (Barnes et al., 2012; Champagnac et al., 2012; Carretier et al., 2013). Unlike the nonlinear increase in the Andes (Barnes et al., 2012; Carretier et al., 2013), we do not observe any sudden change in the erosion rate over time. The erosion history does not show a nonlinear increase during the Taiwan Orogeny.

## 7 Conclusions

New ZFT and ZHe ages from high elevations in the mid-HR are used to construct AERs with a time-dependent thermal model that incorporates erosion. In general, the ensemble average of lower misfit models has a steady increase in the exhumation rate, while models with a late rapid increase in the exhumation rate have larger misfits. All models demonstrate that the region has experienced rapid cooling since 2 Ma, regardless of the exhumation rate history, which indicates that the observations of rapid cooling in the last 2 Ma do not require enhanced exhumation in the same time span. Our results suggest that the mid-HR has undergone progressive crustal thickening, which progressively increases the topographic relief and erosion rate since the onset of the collision.

## Acknowledgments

We would like to thank MOST 110-2116-M-001-005 for funding. We are grateful to Tim Byrne and an anonymous reviewer for their valuable feedback and constructive comments on the study. We thank Tsung-Kwei Liu, Yuan-Hsi Lee, Shao-Yi Huang, and Tzu-Tsen Shen for their technical support. We also thank Timothy Lee, Larry Syu-Heng Lai, and Hsi-An Chen for their assistance in collecting samples in the field.

## Data and Software Availability Statement

The dating data and the code for modeling, data cleaning, and analysis in the research are provided with an MIT License. They are available in *Geoflac for thermochronology with HR2022* (Shyu et al., 2023).

## References

Barnes, J.B., Ehlers, T.A., Insel, N., McQuarrie, N., Poulsen, C.J., 2012. Linking orography, climate, and exhumation across the central Andes. Geology 40 (12), pp. 1135-1138. doi:10.1130/g33229.1.

Barr, T.D., Dahlen, F.A., 1989. Brittle frictional mountain building: 2. Thermal structure and heat budget. Journal of Geophysical Research 94 (B4), p. 3923. doi:10.1029/JB094iB04p03923.

Beyssac, O., Simoes, M., Avouac, J.P., Farley, K.A., Chen, Y.-G., Chan, Y.-C., Goffé, B., 2007. Late Cenozoic metamorphic evolution and exhumation of Taiwan. Tectonics 26 (6), pp. 1-32. doi:10.1029/2006tc002064.

Brandon, M.T., 2007. Programs for Illustrating Closure, Partial Retention, and the Response of Cooling Ages to Erosion: CLOSURE, AGE2EDOT, AND RESPTIME. Yale University.

Brandon, M.T., Roden-Tice, M.K., Garver, J.I., 1998. Late Cenozoic exhumation of the Cascadia accretionary wedge in the Olympic Mountains, northwest Washington State. Geological Society of America Bulletin 110 (8), pp. 985-1009. doi:10.1130/0016-7606(1998)110<0985:lceotc>2.3.co;2.

Braun, J., van der Beek, P., Valla, P., Robert, X., Herman, F., Glotzbach, C., Pedersen, V., Perry, C., Simon-Labric, T., Prigent, C., 2012. Quantifying rates of landscape evolution and tectonic processes by thermochronology and numerical modeling of crustal heat transport using PECUBE. Tectonophysics 524-525, pp. 1-28. doi:10.1016/j.tecto.2011.12.035.

Brown, R.W., Summerfield, M.A., 1997. Some uncertainties in the derivation of rates of denudation from thermochronologic data. Earth Surface Processes and Landforms 22, pp. 239-248. doi:10.1002/(SICI)1096-9837(199703)22:3<239::AID-ESP751>3.0.CO;2-B.

Carena, S., Suppe, J., Kao, H., 2002. Active detachment of Taiwan illuminated by small earthquakes and its control of first-order topography. Geological Society of America Bulletin 30 (10), pp. 935-938. doi:10.1130/0091-7613(2002)030<0935:ADOTIB>2.0.CO;2.

Carretier, S., Regard, V., Vassallo, R., Aguilar, G., Martinod, J., Riquelme, R., Pepin, E., Charrier, R., Hérail, G., Farías, M., Guyot, J.-L., Vargas, G., Lagane, C., 2013. Slope and climate variability control of erosion in the Andes of central Chile. Geology 41 (2), pp. 195-198. doi:10.1130/g33735.1.

Champagnac, J.-D., Molnar, P., Sue, C., Herman, F., 2012. Tectonics, climate, and mountain topography. Journal of Geophysical Research: Solid Earth 117 (B2), pp. n/a-n/a. doi:10.1029/2011jb008348.

Chapple, W.M., 1978. Mechanics of thin-skinned fold-and-thrust belts. GSA Bulletin 89 (8), pp. 1189-1198. doi:10.1130/0016-7606(1978)89<1189:Motfb>2.0.Co;2.

Chen, C.-H., Wang, C.-H., 1995. Explanatory notes for the metamorphic facies map of Taiwan. Central Geological Survey, MOEA, Taipei.

Chen, C.-T., Chan, Y.-C., Lo, C.-H., Malavieille, J., Lu, C.-Y., Tang, J.-T., Lee, Y.-H., 2018. Basal accretion, a major mechanism for mountain building in Taiwan revealed in rock thermal history. Journal of Asian Earth Sciences 152, pp. 80-90. doi:10.1016/j.jseaes.2017.11.030.

Chen, W.-S., Yeh, J.-J., Syu, S.-J., 2019. Late Cenozoic exhumation and erosion of the Taiwan orogenic belt: New insights from petrographic analysis of foreland basin sediments and thermochronological dating on the metamorphic orogenic wedge. Tectonophysics 750, pp. 56-69. doi:10.1016/j.tecto.2018.09.003.

Clark, M.B., Fisher, D.M., Lu, C.-Y., Chen, C.-H., 1993. Kinematic analyses of the Hsüehshan Range, Taiwan: A large-scale pop-up structure. Tectonics 12 (1), pp. 205-217. doi:10.1029/92TC01711.

Coutand, I., Whipp, D.M., Grujic, D., Bernet, M., Fellin, M.G., Bookhagen, B., Landry, K.R., Ghalley, S.K., Duncan, C., 2014. Geometry and kinematics of the Main Himalayan Thrust and Neogene crustal exhumation in the Bhutanese Himalaya derived from inversion of multithermochronologic data. Journal of Geophysical Research: Solid Earth 119 (2), pp. 1446-1481. doi:10.1002/2013jb010891.

Cundall, P.A., 1989. Numerical experiments on localization in frictional materials. Ingenieur-Archiv 59, pp. 148-159. doi:10.1007/BF00538368.

Dadson, S.J., Hovius, N., Chen, H., Dade, W.B., Hsieh, M.-L., Willett, S.D., Hu, J.-C., Horng, M.-J., Chen, M.-C., Stark, C.P., Lague, D., Lin, J.-C., 2003. Links between erosion, runoff variability and seismicity in the Taiwan orogen. Nature 426 (6967), pp. 648-651. doi:10.1038/nature02150.

Dai, J.G., Fox, M., Han, X., Tremblay, M.M., Xu, S.Y., Shuster, D.L., Liu, B.R., Zhang, J., Wang, C.S., 2021. Two Stages of Accelerated Exhumation in the Middle Reach of the Yarlung River, Southern Tibet Since the Mid-Miocene. Tectonics 40 (6). doi:10.1029/2020tc006618.

Das, P., Lin, A.T.-S., Chen, M.-P.P., Miramontes, E., Liu, C.-S., Huang, N.-W., Kung, J., Hsu, S.-K., Pillutla, R.K., Nayak, K., 2021. Deep-sea submarine erosion by the Kuroshio Current in the Manila accretionary prism, offshore Southern Taiwan. Tectonophysics 807. doi:10.1016/j.tecto.2021.228813.

Davis, D., Suppe, J., Dahlen, F.A., 1983. Mechanics of fold-and-thrust belts and accretionary wedges. Journal of Geophysical Research 88 (B2), pp. 1153-1172. doi:10.1029/JB088iB02p01153.

Deffontaines, B., Lee, J.-C., Angelier, J., Carvalho, J., Rudant, J.-P., 1994. New geomorphic data on the active Taiwan orogen: A multisource approach. Journal of Geophysical Research: Solid Earth 99 (B10), pp. 20243-20266. doi:10.1029/94jb00733.

Derrieux, F., Siame, L.L., Bourlès, D.L., Chen, R.-F., Braucher, R., Léanni, L., Lee, J.-C., Chu, H.-T., Byrne, T.B., 2014. How fast is the denudation of the Taiwan mountain belt? Perspectives from in situ cosmogenic 10Be. Journal of Asian Earth Sciences 88, pp. 230-245. doi:10.1016/j.jseaes.2014.03.012.

674 Dobson, K.J., Stuart, F.M., Dempster, T.J., 2008. U and Th zonation in Fish Canyon Tuff
675 zircons: Implications for a zircon (U–Th)/He standard. Geochimica et Cosmochimica
676 Acta 72 (19), pp. 4745-4755. doi:10.1016/j.gca.2008.07.015.

677 Dodson, M.H., 1973. Closure temperature in cooling geochronological and petrological
678 systems. Contribution to Mineralogy and Petrology 40, pp. 259-274.
679 doi:10.1007/BF00373790.

680 Dodson, M.H., 1979. Theory of Cooling ages, in: Jager, E., Hunziker, J.C. (Eds.), Lecture in
681 Isotope Geology. Springer-Verlag, New York, pp. 194-206. doi:10.1007/978-3-642-
682 67161-6_14.

683 Fellin, M.G., Chen, C.-Y., Willett, S.D., Christl, M., Chen, Y.-G., 2017. Erosion rates across
684 space and timescales from a multi-proxy study of rivers of eastern Taiwan. Global and
685 Planetary Change 157, pp. 174-193. doi:10.1016/j.gloplacha.2017.07.012.

686 Foeken, J.P.T., Stuart, F.M., Dobson, K.J., Persano, C., Vilbert, D., 2006. A diode laser
687 system for heating minerals for (U-Th)/He chronometry. Geochemistry, Geophysics,
688 Geosystems 7 (4). doi:10.1029/2005gc001190.

689 Fox, M., Bodin, T., Shuster, D.L., 2015. Abrupt changes in the rate of Andean Plateau uplift
690 from reversible jump Markov Chain Monte Carlo inversion of river profiles.
691 Geomorphology 238, pp. 1-14. doi:10.1016/j.geomorph.2015.02.022.

692 Fox, M., Reverman, R., Herman, F., Fellin, M.G., Sternai, P., Willett, S.D., 2014. Rock uplift
693 and erosion rate history of the Bergell intrusion from the inversion of low temperature
694 thermochronometric data. Geochemistry, Geophysics, Geosystems 15 (4), pp. 1235-
695 1257. doi:10.1002/2013gc005224.

696 Fuller, C.W., Willett, S.D., Fisher, D., Lu, C.Y., 2006. A thermomechanical wedge model of
697 Taiwan constrained by fission-track thermochronometry. Tectonophysics 425 (1-4),
698 pp. 1-24. doi:10.1016/j.tecto.2006.05.018.

699 Galewsky, J., Stark, C.P., Dadson, S., Wu, C.C., Sobel, A.H., Horng, M.J., 2006. Tropical
700 cyclone triggering of sediment discharge in Taiwan. Journal of Geophysical Research:
701 Earth Surface 111 (F3). doi:10.1029/2005jf000428.

702 Gérard, B., Robert, X., Grujic, D., Gautheron, C., Audin, L., Bernet, M., Balvay, M., 2022.
703 Zircon (U-Th)/He Closure Temperature Lower Than Apatite Thermochronometric
704 Systems: Reconciliation of a Paradox. Minerals 12 (2). doi:10.3390/min12020145.

705 Ho, C.S., 1986. A synthesis of the geologic evolution of Taiwan. Tectonophysics 125 (1), pp.
706 1-16. doi:10.1016/0040-1951(86)90004-1.

707 Hourigan, J.K., Reiners, P.W., Brandon, M.T., 2005. U-Th zonation-dependent alpha-
708 ejection in (U-Th)/He chronometry. Geochimica et Cosmochimica Acta 69 (13), pp.
709 3349-3365. doi:10.1016/j.gca.2005.01.024.

710 Hsieh, H.-H., Chen, C.-H., Lin, P.-Y., Yen, H.-Y., 2014. Curie point depth from spectral
711 analysis of magnetic data in Taiwan. Journal of Asian Earth Sciences 90, pp. 26-33.
712 doi:10.1016/j.jseaes.2014.04.007.

Hsu, W.-H., Byrne, T.B., Ouimet, W., Lee, Y.-H., Chen, Y.-G., Soest, M.v., Hodges, K., 2016. Pleistocene onset of rapid, punctuated exhumation in the eastern Central Range of the Taiwan orogenic belt. Geology 44 (9), pp. 719-722. doi:10.1130/g37914.1.

Huang, S.-Y., Lee, Y.-H., Mesalles, L., Horng, C.-S., Lu, H.-Y., Tsai, Y.-L., Wu, Y.-J., Chen, F.-Y., Tan, X.-B., 2022. Plio-Pleistocene fluvial dynamics in the pro-foreland basins of Taiwan: Thermochronological constraints and tectonic implications from the syn-orogenic deposits. Tectonophysics 838. doi:10.1016/j.tecto.2022.229486.

Huang, T.-Y., Gung, Y., Kuo, B.-Y., Chiao, L.-Y., Chen, Y.-N., 2015. Layered deformation in the Taiwan orogen. Science 349 (6249), pp. 720-723. doi:10.1126/science.aab1879.

Hung, J.-H., Wiltschko, D.V., Lin, H.-C., Hickman, J.B., Fang, P., Bock, Y., 1999. Structure and motion of the southwestern Taiwan fold and thrust belt. Terrestrial Atmospheric and Oceanic Sciences 10, pp. 543-568. doi:10.3319/TAO.1999.10.3.543(T).

Hurford, A.J., 1986. Cooling and uplift patterns in the Lepontine Alps South Central Switzerland and an age of vertical movement on the Insubric fault line. Contributions to Mineralogy and Petrology 92 (4), pp. 413-427. doi:10.1007/BF00374424.

Hurford, A.J., Green, P.F., 1983. The zeta age calibration of fission-track dating. Chemical Geology 41 (0), pp. 285-317. doi:10.1016/S0009-2541(83)80026-6.

Kidder, S., Avouac, J.-P., Chan, Y.-C., 2012. Constraints from rocks in the Taiwan orogen on crustal stress levels and rheology. Journal of Geophysical Research 117 (B9), p. 13. doi:10.1029/2012jb009303.

Kirstein, L.A., Carter, A., Chen, Y.-G., 2013. Impacts of arc collision on small orogens: new insights from the Coastal Range detrital record, Taiwan. Journal of the Geological Society 171 (1), pp. 5-8. doi:10.1144/jgs2013-046.

Kirstein, L.A., Fellin, M.G., Willett, S.D., Carter, A., Chen, Y.-G., Garver, J.I., Lee, D.-C., 2010. Pliocene onset of rapid exhumation in Taiwan during arc-continent collision: new insights from detrital thermochronometry. Basin Research 22 (3), pp. 270-285. doi:10.1111/j.1365-2117.2009.00426.x.

Lan, C.-H., 2009, Fission track dating of zircon from the middle Hsuehshan Range of Taiwan, Master Thesis, National Chung Cheng University, 72. Retrieved from https://hdl.handle.net/11296/q4s3n6.

Lee, C.R., Cheng, W.T., 1986. Preliminary heat flow measurements in Taiwan, paper presented at Fourth Circum-Pacific Energy and Mineral Resources Conference, Circum-Pac. Counc. for Energy and Miner. Resour., Singapore, pp. 1-9.

Lee, J.-C., Angelier, J., Chu, H.-T., 1997. Polyphase history and kinematics of a complex major fault zone in the northern Taiwan mountain belt: the Lishan Fault. Tectonophysics 274 (1–3), pp. 97-115. doi:10.1016/S0040-1951(96)00300-9.

Lee, Y.-H., Byrne, T.B., Lo, W., Wang, S.-J., Tsao, S.-J., Chen, C.-H., Yu, H.-C., Tan, X., van Soest, M., Hodges, K., Mesalles, L., Robinson, H., Fosdick, J.C., 2022. Out of sequence faulting in the backbone range, Taiwan: Implications for thickening and

752 exhumation processes. Earth and Planetary Science Letters 594.
753 doi:10.1016/j.epsl.2022.117711.

754 Lee, Y.-H., Chen, C.-C., Liu, T.-K., Ho, H.-C., Lu, H.-Y., Lo, W., 2006. Mountain building
755 mechanisms in the Southern Central Range of the Taiwan Orogenic Belt — From
756 accretionary wedge deformation to arc–continental collision. Earth and Planetary
757 Science Letters 252 (3-4), pp. 413-422. doi:10.1016/j.epsl.2006.09.047.

758 Lee, Y.H., Byrne, T., Wang, W.H., Lo, W., Rau, R.J., Lu, H.Y., 2015. Simultaneous
759 mountain building in the Taiwan orogenic belt. Geology 43 (5), pp. 451-454.
760 doi:10.1130/g36373.1.

761 Liang, J.-H., 2011, Zircon and apatite fission track dating along the "Lishan fault" and its
762 tectonic implication, Master Thesis, National Chung Cheng University, 55. Retrieved
763 from https://hdl.handle.net/11296/n6auhr.

764 Lin, A.T., Watts, A.B., Hesselbo, S.P., 2003. Cenozoic stratigraphy and subsidence history of
765 the South China Sea margin in the Taiwan region. Basin Research 15 (4), pp. 453-
766 478. doi:10.1046/j.1365-2117.2003.00215.x.

767 Liu, C.-M., Song, S.-R., Kuo, C.-H., 2015. Silica Geothermometry Applications in the
768 Taiwan Orogenic Belt. Terrestrial, Atmospheric and Oceanic Sciences 26 (4).
769 doi:10.3319/tao.2015.02.09.01(tt).

770 Liu, H.-C., Kao, M.-C., 2011. Geological map of Taiwan scale 1:50,000: Lishan. Central
771 Geological Survey, MOEA, Taipei.

772 Liu, H.-C., Lin, C.-W., Yang, C.-N., 2009. On the Stratigraphy and Geological Structures in
773 Upper Reaches of the Ta-anchi River, Central Taiwan. Bulletin of the Central
774 Geological Survey 22, pp. 29-61.

775 Liu, T.-K., 1982. Tectonic implication of fission track ages from the Central Range, Taiwan,
776 Proc. Geol. Soc. China, pp. 22-37.

777 Liu, T.-K., Chen, Y.-G., Chen, W.-S., Jiang, S.-H., 2000. Rates of cooling and denudation of
778 the Early Penglai Orogeny, Taiwan, as assessed by fission-track constraints.
779 Tectonophysics 320, pp. 69-82. doi:10.1016/S0040-1951(00)00028-7.

780 Liu, T.-K., Hsieh, S., Chen, Y.-G., Chen, W.-S., 2001. Thermo-kinematic evolution of the
781 Taiwan oblique-collision mountain belt as revealed by zircon fission track dating.
782 Earth and Planetary Science Letters 186, pp. 45-56. doi:10.1016/S0012-
783 821X(01)00232-1.

784 Lo, C.H., Yui, T.F.U., 1996. 40Ar/39Ar dating of high-pressure rocks in the tananao
785 basement complex, Taiwan. J. Geol. Soc. China 39 (1), pp. 13-30.

786 Lock, J., 2007, Interpreting low-temperature thermochronometric data in fold-and-thrust
787 belts: An example from the Western Foothills, Taiwan, Ph.D. Thesis, University of
788 Washington, 204. Retrieved from
789 http://gateway.proquest.com/openurl?url_ver=Z39.88-
790 2004&rft_val_fmt=info:ofi/fmt:kev:mtx:dissertation&res_dat=xri:pqdiss&rft_dat=xri:
791 pqdiss:3290562.

Maino, M., Gaggero, L., Langone, A., Seno, S., Fanning, M., 2019. Cambro-Silurian magmatisms at the northern Gondwana margin (Penninic basement of the Ligurian Alps). Geoscience Frontiers 10 (1), pp. 315-330. doi:10.1016/j.gsf.2018.01.003.

Mancktelow, N.S., Grasemann, B., 1997. Time-dependent effects of heat advection and topography on cooling histories during erosion. Tectonophysics 270 (3–4), pp. 167-195. doi:10.1016/S0040-1951(96)00279-X.

McCallister, A.T., Taylor, M.H., Murphy, M.A., Styron, R.H., Stockli, D.F., 2014. Thermochronologic constraints on the late Cenozoic exhumation history of the Gurla Mandhata metamorphic core complex, Southwestern Tibet. Tectonics 33 (2), pp. 27-52. doi:10.1002/2013tc003302.

Meesters, A.G.C.A., Dunai, T.J., 2005. A noniterative solution of the (U-Th)/He age equation. Geochemistry, Geophysics, Geosystems 6 (4). doi:10.1029/2004gc000834.

Molnar, P., England, P., Martinod, J., 1993. Mantle dynamics, uplift of the Tibetan Plateau, and the Indian Monsoon. Reviews of Geophysics 31 (4), pp. 357-396. doi:10.1029/93RG02030.

Montgomery, D.R., Brandon, M.T., 2002. Topographic controls on erosion rates in tectonically active mountain ranges. Earth and Planetary Science Letters 201 (3), pp. 481-489. doi:10.1016/S0012-821X(02)00725-2.

Mouthereau, F., Lacombe, O., Deffontaines, B., Angelier, J., Brusset, S., 2001. Deformation history of the southwestern Taiwan foreland thrust belt: insights from tectono-sedimentary analyses and balanced cross-sections. Tectonophysics 333. doi:10.1016/S0040-1951(00)00280-8.

Reiners, P.W., Spell, T.L., Nicolescu, S., Zanetti, K.A., 2004. Zircon (U-Th)/He thermochronometry: He diffusion and comparisons with 40Ar/39Ar dating. Geochimica et Cosmochimica Acta 68 (8), pp. 1857-1887. doi:10.1016/j.gca.2003.10.021.

Shyu, C.J., Tan, E., Lavier, L.L., 2023, Geoflac for thermochronology with HR2022 (Version 1.0.3). Zenodo. doi:10.5281/zenodo.7816507.

Shyu, J.B.H., Sieh, K., 2005. Neotectonic architecture of Taiwan and its implications for future large earthquakes. Journal of Geophysical Research 110 (B8). doi:10.1029/2004jb003251.

Simoes, M., Avouac, J.P., Beyssac, O., Goffé, B., Farley, K.A., Chen, Y.-G., 2007. Mountain building in Taiwan: A thermokinematic model. Journal of Geophysical Research 112 (B11), p. 25. doi:10.1029/2006jb004824.

Stolar, D.B., Willett, S.D., Montgomery, D.R., 2007. Characterization of topographic steady state in Taiwan. Earth and Planetary Science Letters 261 (3-4), pp. 421-431. doi:10.1016/j.epsl.2007.07.045.

Suppe, J., 1981. Mechanics of mountain building and metamorphism in Taiwan. Memoir of the Geological Society of China (4), pp. 67-89.

Suppe, J., 1984. Kinematics of Arc-Continent Collision, Flipping of Subduction, and Back-Arc Spreading Near Taiwan. Memoir of the Geological Society of China (6), pp. 21-33.

Tan, E., Lavier, L.L., Van Avendonk, H.J.A., Heuret, A., 2012. The role of frictional strength on plate coupling at the subduction interface. Geochemistry, Geophysics, Geosystems 13 (10), p. 19. doi:10.1029/2012gc004214.

Teng, L.S., 1987. Stratigraphic records of the late Cenozoic Penglai orogeny of Taiwan. Acta Geologica Taiwanica (25), pp. 205-224.

Teng, L.S., 1990. Geotectonic evolution of late Cenozoic arc-continent collision in Taiwan. Tectonophysics 183 (1–4), pp. 57-76. doi:10.1016/0040-1951(90)90188-E.

Teng, L.S., 1992. Geotectonic Evolution of Tertiary Continental Margin Basins of Taiwan. Petroleum Geology of Taiwan 27, pp. 1-19.

Teng, L.S., 2007. Quaternary Tectonics of Taiwan. Special Publication of the Central Geological Survey 18, pp. 1-24.

Tillman, K.S., Byrne, T.B., 1995. Kinematic analysis of the Taiwan Slate Belt. Tectonics 14 (2), pp. 322-341. doi:10.1029/94tc02451.

Tsao, S., 1996, The geological significances of illite crystallinity, zircon fission-track ages, and K-Ar ages of metasedimentary rocks of the Central Range of Taiwan, Ph.D. Thesis, National Taiwan University, 272. Retrieved from https://hdl.handle.net/11296/aykz26.

van der Beek, P., Schildgen, T.F., 2023. Short communication: age2exhume – a MATLAB/Python script to calculate steady-state vertical exhumation rates from thermochronometric ages and application to the Himalaya. Geochronology 5 (1), pp. 35-49. doi:10.5194/gchron-5-35-2023.

Willett, S.D., Brandon, M.T., 2002. On steady states in mountain belts. GSA. doi:10.1130/0091-7613(2002)030<0175:OSSIMB>2.0.CO;2.

Willett, S.D., Fisher, D., Fuller, C., Yeh, E.-C., Lu, C.-Y., 2003. Erosion rates and orogenic-wedge kinematics in Taiwan inferred from fission-track thermochronometry. Geology 31 (11), pp. 945-948. doi:10.1130/G19702.1.

Wolff, R., Hetzel, R., Dunkl, I., Anczkiewicz, A.A., Pomella, H., 2020. Fast cooling of normal-fault footwalls: Rapid fault slip or thermal relaxation? Geology 48 (4), pp. 333-337. doi:10.1130/g46940.1.

Wu, S.-K., Chi, W.-C., Hsu, S.-M., Ke, C.-C., Wang, Y., 2013. Shallow crustal thermal structures of central Taiwan foothills region. Terr. Atmos. Ocean. Sci. 24 (4), pp. 695-707. doi:10.3319/TAO.2013.03.13.01(T).

Wu, Y.-J., 2018, Detrital Zircon Fission-Track and U-Pb Dating of the Toukoshan and Cholan Formations in Central Taiwan and its Tectonic Implications, Master Thesis, National Chung Cheng University, 77. Retrieved from https://hdl.handle.net/11296/w4mg2h.

Yeh, J.-J., 2017, Petrographic study of the Miocene-Pleistocene sandstone in the Western Foothills, northern Taiwan: implication for the unroofing history of Taiwan orogenic belt, Master Thesis, National Taiwan University, 116. doi:10.6342/NTU201703422.

Yu, P.-S., Yang, T.-C., Kuo, C.-C., 2006. Evaluating Long-Term Trends in Annual and Seasonal Precipitation in Taiwan. Water Resources Management 20 (6), pp. 1007-1023. doi:10.1007/s11269-006-9020-8.

Yu, S.-B., Chen, H.-Y., Kuo, L.-C., 1997. Velocity field of GPS stations in the Taiwan area. Tectonophysics 274, pp. 41-59. doi:10.1016/S0040-1951(96)00297-1.

Yue, L.-F., Suppe, J., Hung, J.-H., 2005. Structural geology of a classic thrust belt earthquake: the 1999 Chi-Chi earthquake Taiwan (Mw=7.6). Journal of Structural Geology 27 (11), pp. 2058-2083. doi:10.1016/j.jsg.2005.05.020.

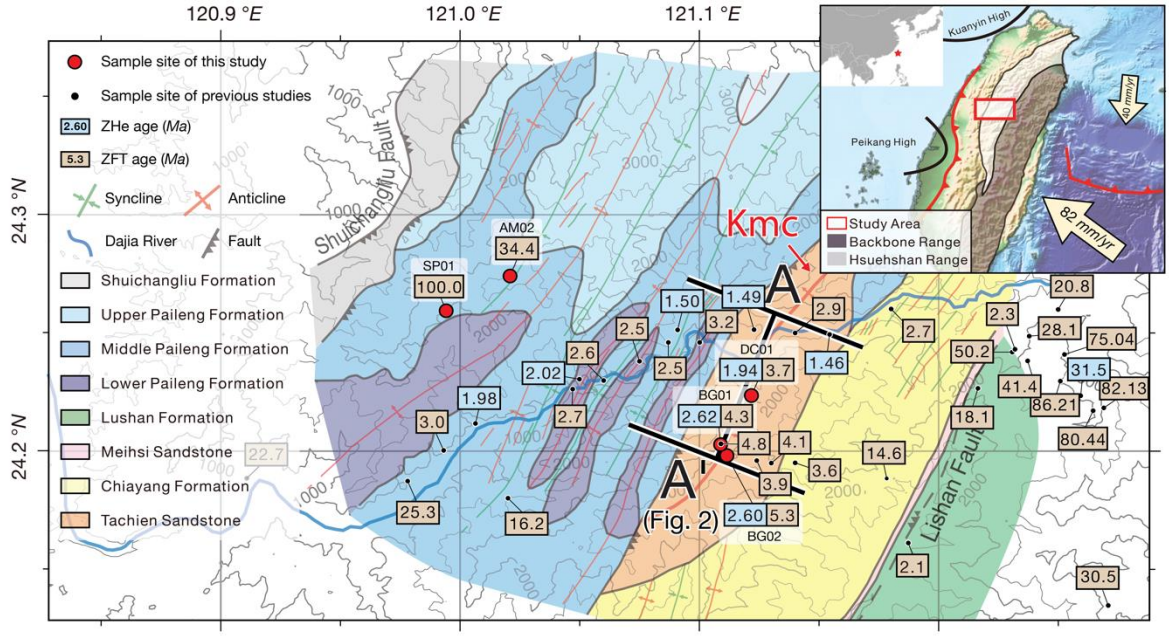


883

884 **Figure 1.** Geological formations and structural framework (Liu and Kao, 2010) of the study
885 area. The inset shows the location of Taiwan and the study area (red rectangle) in the mid-HR
886 range. The A-A' profile is located along the Kuangmingchiao (Kmc) Anticlinorium. The
887 cooling ages from this study (red circles) are shown along with data from previous studies
888 (Tsao, 1996; Liu et al., 2001; Fuller et al., 2006; Lee et al., 2006; Beyssac et al., 2007; Lan,
889 2009; Liang, 2011; Lee et al., 2015).

890

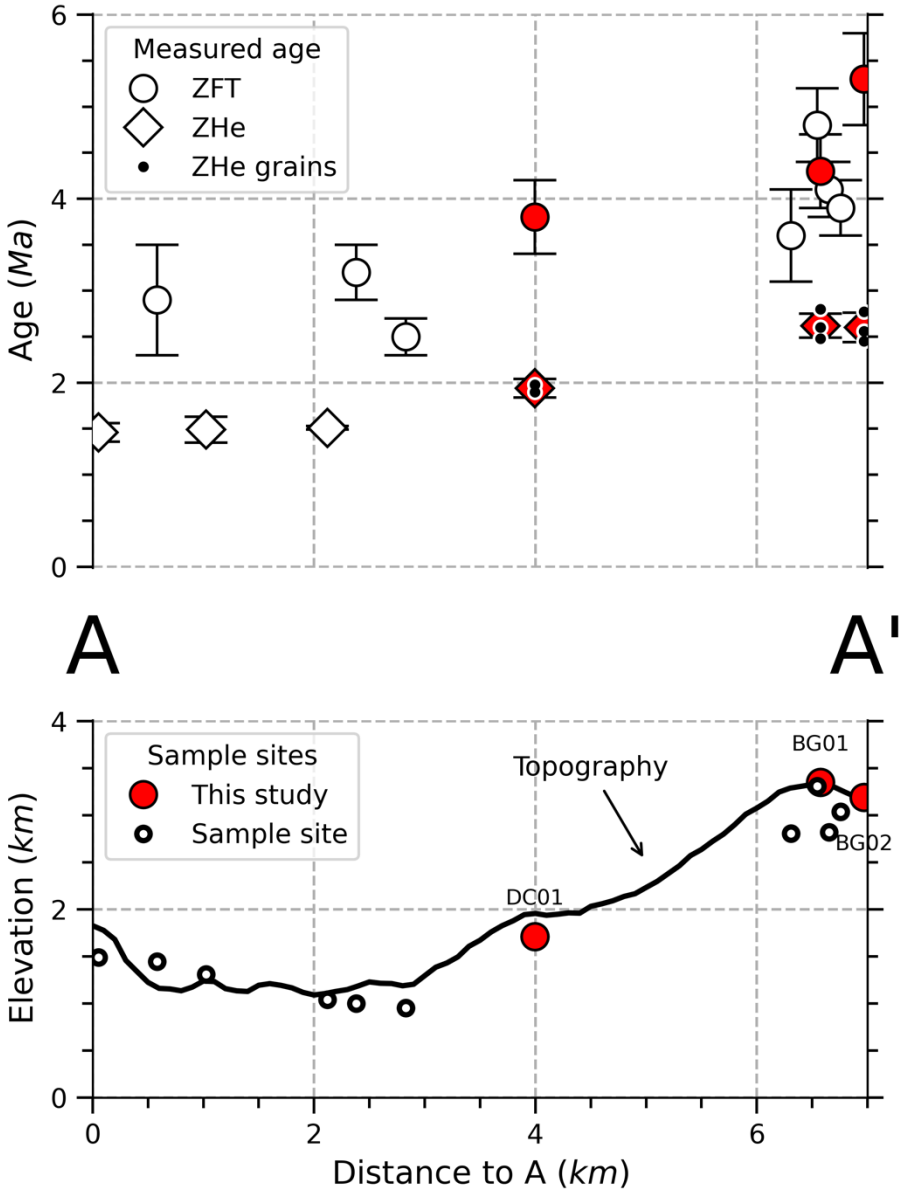


**Figure 2.** Cooling ages (upper panel) and topography (lower panel) along the A-A' profile are shown in Figure 1. The three high-elevation samples (red circles) were dated by the ZFT and ZHe methods in this study (Table 1). Ten samples (open circles) from previous studies (Table 2) are shown.

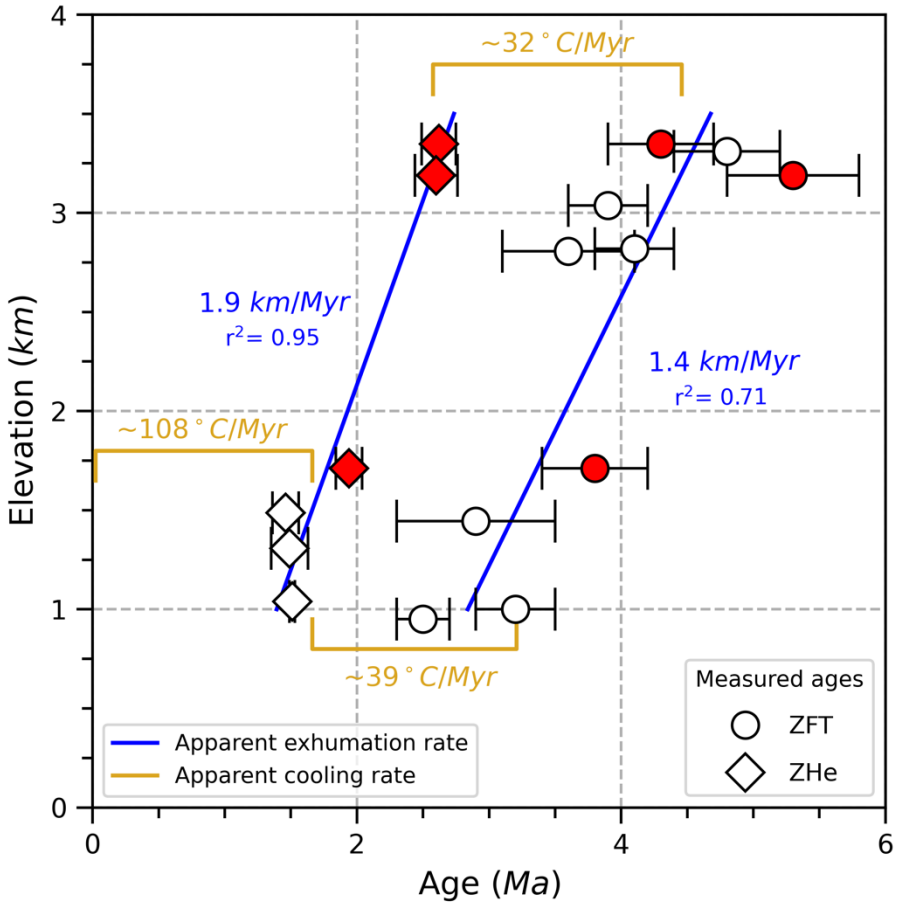


**Figure 3.** ZFT and ZHe cooling ages vs. elevation of samples from along the A-A' profile. Red symbols are from this study, and open symbols are from previous studies (Table 2). The linear regressions (blue lines) of the data show the apparent exhumation rates. The temporal change in the cooling rate is indicated in yellow.

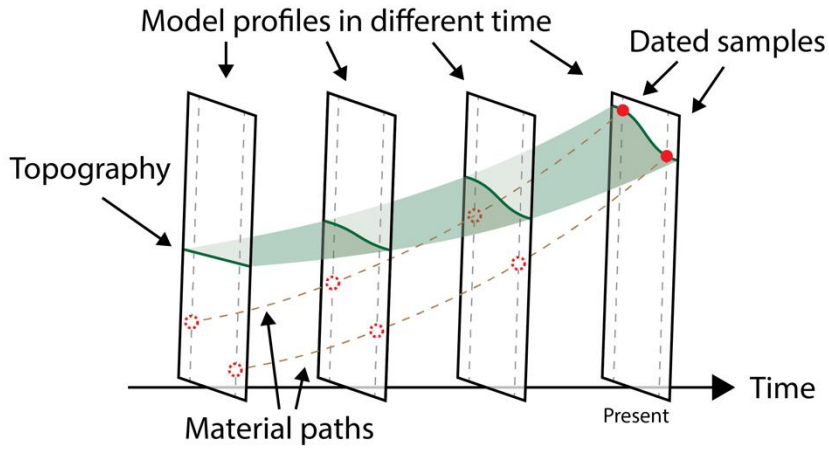


**Figure 4.** Schematic diagram of exhumation in the 2D thermal models. The tectonic uplift elevates the rock while the surface is eroded, which exhumes the rock to the surface.

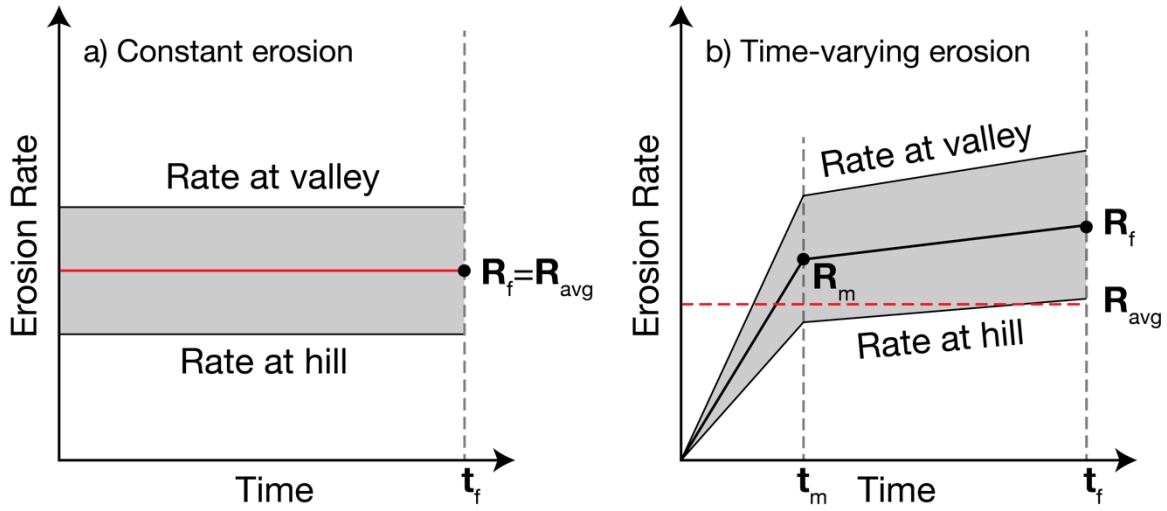


908

909 **Figure 5.** Two evolution scenarios, where a) the erosion rate stays constant and b) the erosion
910 rate has a time-varying increase (or decrease). The thick black lines are the spatially averaged
911 erosion rates, R(t). The thin black lines above and below are the erosion rates at the valley and
912 hill, respectively. $t_m$ is the duration of the first stage, and $t_f$ is the duration of the simulation (6
913 or 7 Myr). $R_f$ is the value of R(t) at the end of the simulation. $R_m$ is the value of R(t) at $t_m$.
914 $r_m$=$R_m$/$R_f$ is the ratio between the rates at the end of the first stage and the second stage. $R_{avg}$ is
915 the time-averaged erosion rate. The integration over the shaded area is the topographic relief
916 between the valley and hill.

917

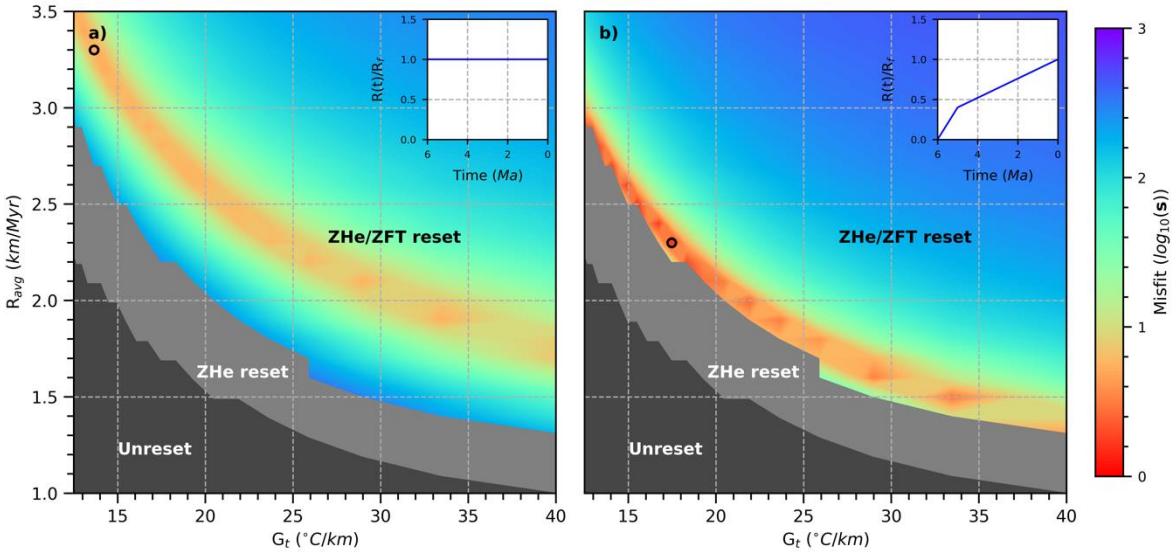


**Figure 6.** Misfits of the a) constant-erosion scenario (Series 1 in Table 3) and b) best-fit series in the time-varying scenario (Series 6 in Table 3). Within each series, the initial geothermal gradient ($G_t$) and the time-averaged erosion rate ($R_{avg}$) are varied. Black circles are the minimum misfit of each series. Dark gray indicates the models with unreset ZHe and ZFT values at the surface. Light gray indicates the models with unreset ZHe values at the surface. Insets are the relative erosion rate history of each series.

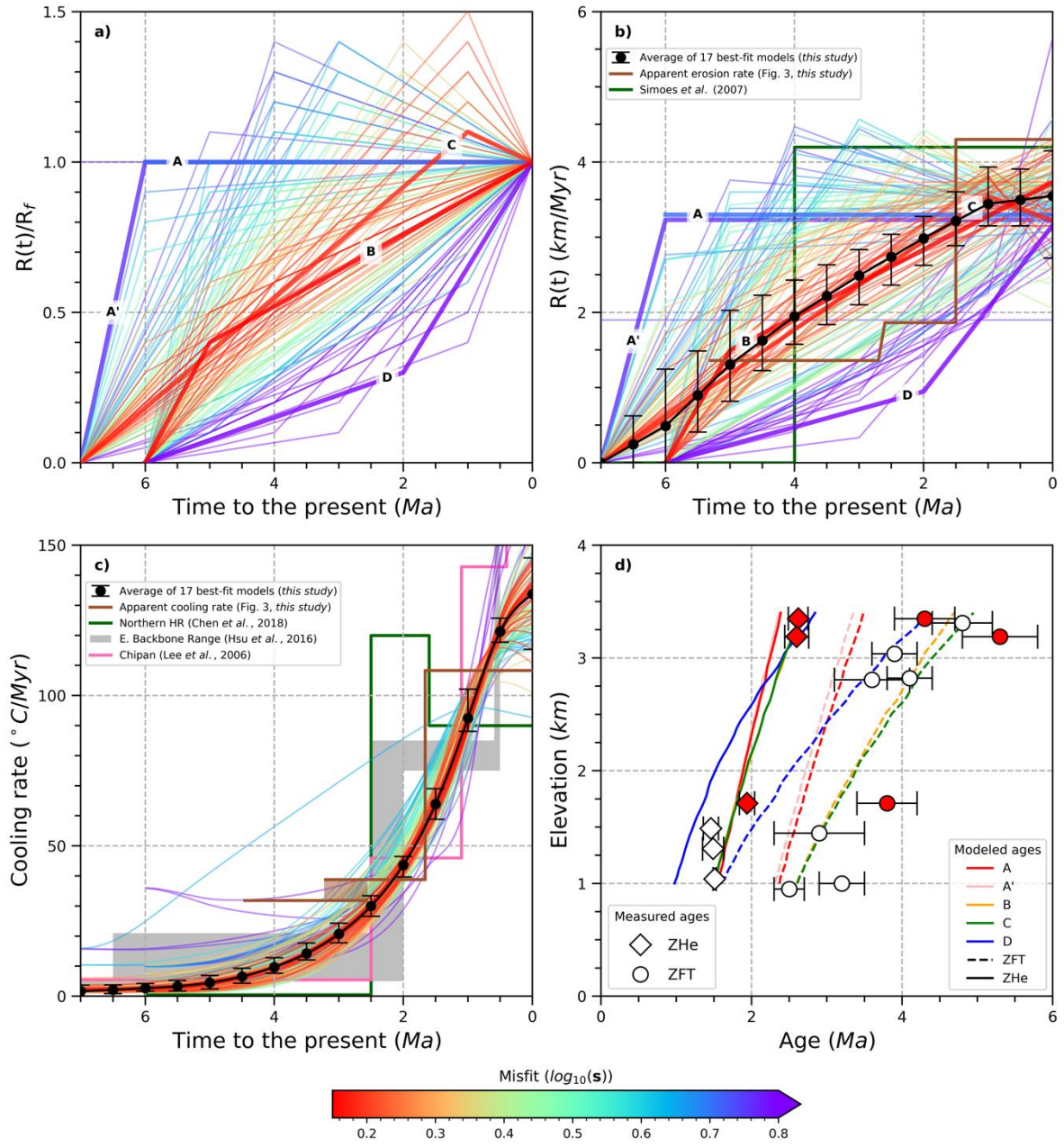


**Figure 7.** Erosion rate, cooling rates, and AER of the model results. a) Relative erosion rate, $R(t)/R_f$, which is color-coded with model misfits. Labels A-D indicate the four representative models in the main text. b) Erosion rate, R(t), which is color-coded with misfits and exhumation/erosion rates estimated by different methods. c) Cooling rate, which is color-coded with model misfits. d) Modeled AERs of the four representative models. Dashed lines indicate modeled ZFT ages. Solid lines indicate modeled ZHe ages. Red/open symbols are ages from this/previous studies. Model A' is used for comparison with Model A, which has similar values of $G_t$ and a constant erosion rate after 6 Ma but has an earlier onset of erosion rate from 0 km/Myr at 7 Ma. A detailed discussion is provided in Section 6.5.

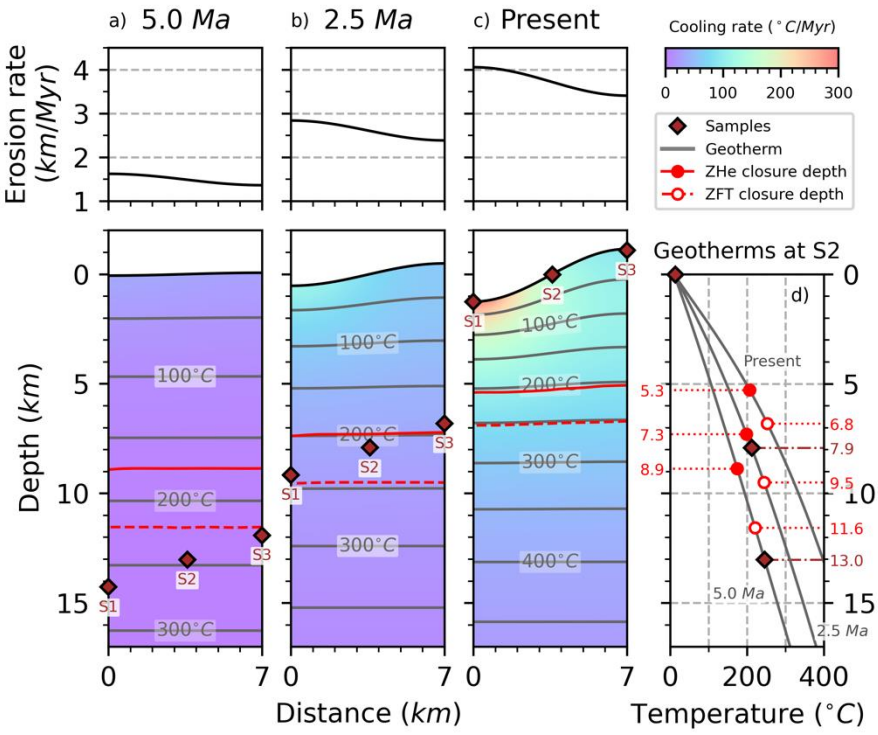


937

938 **Figure 8.** Thermal evolution of Model B. The erosion rate, geotherm, cooling rate, and closure
939 depth at a) 5.0 Ma, b) 2.5 Ma, and c) present. S1-S3 are samples for the model AER. d)
940 Geothermal profiles at S2 at different times. Numbers indicate the depths of S2 and closure
941 depths of ZFT and ZHe.

942

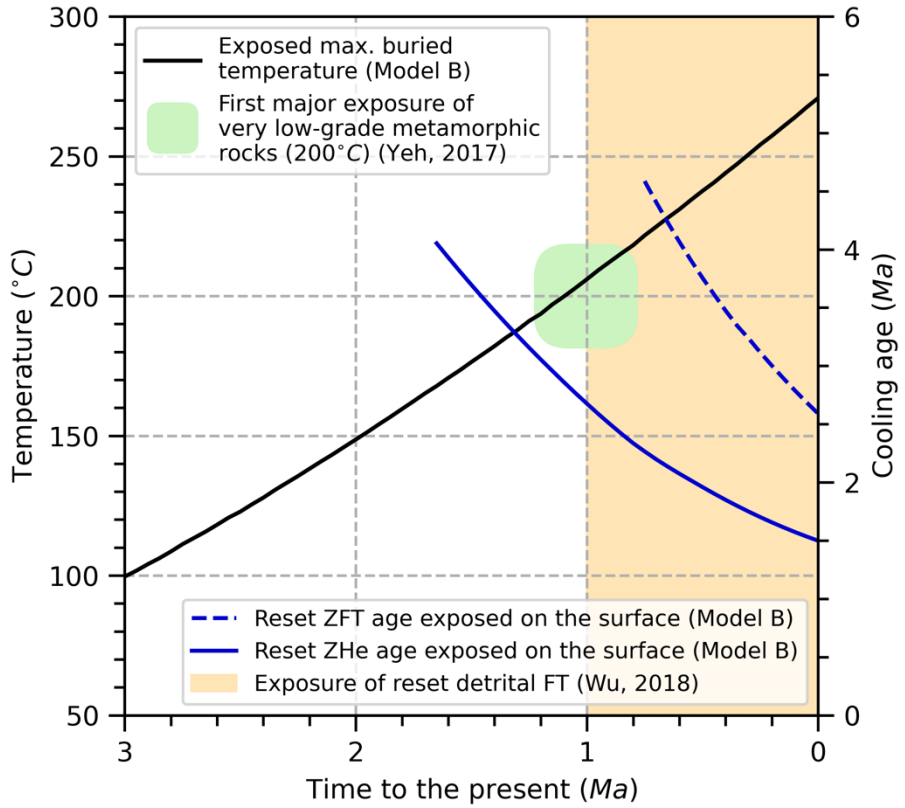


943

944 **Figure 9.** The exposure history of reset ZHe/ZFT ages and the maximum burial temperature
945 in Model B.

946

947

948

949 Table 1. New ZFT and ZHe ages in this study.

**ZFT**

| Sample | Location | | Altitude | $Rho_s$ | $N_s$ | $Rho_i$ | $N_i$ | $Rho_d$ | $N_d$ | Grains | Q | Pooled age | Central age |
|---|---|---|---|---|---|---|---|---|---|---|---|---|---|
| | Lon ($°E$) | Lat ($°N$) | ($m$) | ($cm^{-2}$) | | ($cm^{-2}$) | | ($cm^{-2}$) | | | | ($\pm1\sigma, Ma$) | ($\pm1\sigma, Ma$) |
| SP01 | 120.994 | 24.259 | 2093 | 123.815E+5 | 1071 | 20.347E+5 | 176 | 11.0E+5 | 26 | 10 | 0.15 | 99.6 (±22.2) | 100.0 (±23.2) |
| AM02 | 121.021 | 24.274 | 2581 | 58.233E+5 | 1664 | 24.217E+5 | 692 | 11.0E+5 | 26 | 22 | 0.28 | 39.6 (±8.4) | 34.4 (±8.4) |
| BG01* | 121.109 | 24.203 | 3348 | 9.596E+5 | 730 | 40.670E+5 | 3094 | 12.2E+5 | 4798 | 31 | 0.48 | 4.3 (±0.3) | 4.3 (±0.4) |
| BG02* | 121.111 | 24.198 | 3189 | 1.688E+5 | 774 | 5.850E+5 | 2683 | 12.2E+5 | 4798 | 28 | 0.73 | 5.3 (±0.4) | 5.3 (±0.5) |
| DC01* | 121.122 | 24.223 | 1711 | 6.190E+5 | 462 | 34.203E+5 | 2259 | 12.2E+5 | 4798 | 17 | 0.52 | 3.7 (±0.3) | 3.8 (±0.4) |

**ZHe**

| sample | Rep. | Dimensions | | | Radius | Term. | $^{238}U$ | $^{232}Th$ | $^{4}He$ | Ft | Raw Age | Corrected Age |
|---|---|---|---|---|---|---|---|---|---|---|---|---|
| | | X ($\mu m$) | Y ($\mu m$) | Z ($\mu m$) | ($\mu m$) | (#) | ($ng$) | ($ng$) | ($ncm^3$) | | ($Ma$) | ($\pm1\sigma, Ma$) |
| BG01 | A | 220 | 85 | 80 | 92 | 1 | 3.474 | 2.224 | 0.91 | 0.72 | 1.87 | 2.60 (±0.13) |
| | B | 200 | 100 | 75 | 100 | 2 | 1.073 | 1.563 | 0.34 | 0.75 | 1.95 | 2.60 (±0.13) |
| | C | 190 | 125 | 120 | 113 | 2 | 5.317 | 4.226 | 1.69 | 0.79 | 2.20 | 2.80 (±0.14) |
| | D | 210 | 90 | 80 | 95 | 2 | 3.318 | 7.043 | 1.10 | 0.73 | 1.81 | 2.48 (±0.12) |
| | mean | | | | | | | | | | | **2.62 (±0.13)** |
| BG02 | A | 230 | 100 | 75 | 105 | 2 | 5.737 | 4.299 | 1.52 | 0.76 | 1.86 | 2.45 (±0.12) |
| | B | 200 | 80 | 80 | 86 | 1.5 | 2.244 | 0.721 | 0.57 | 0.70 | 1.94 | 2.77 (±0.14) |
| | C | 200 | 90 | 80 | 93 | 2 | 1.278 | 1.930 | 0.39 | 0.73 | 1.87 | 2.56 (±0.13) |
| | mean | | | | | | | | | | | **2.60 (±0.16)** |
| DC01 | A | 240 | 140 | 100 | 133 | 1 | 3.412 | 3.575 | 0.84 | 0.82 | 1.62 | 1.98 (±0.10) |
| | B | 350 | 240 | 170 | 214 | 2 | 13.335 | 5.359 | 2.99 | 0.89 | 1.68 | 1.90 (±0.09) |
| | $C^+$ | 190 | 110 | 100 | 105 | 2 | 0.249 | 0.273 | 0.33 | 0.77 | 8.55 | 11.17 (±0.56) |
| | mean | | | | | | | | | | | **1.94 (±0.10)** |

950 Location: In the WGS84 system, $Rho_s$ is the density of spontaneous tracks, $N_s$ is the number
951 of spontaneous tracks, $Rho_i$ is the density of induced tracks, $N_i$ is the number of induced tracks,
952 Rho$_d$ is the density of dosimeter tracks, $N_d$ is the number of dosimeter tracks, Q is the $\chi^2$
953 probability, Rep. is the replicate, Term. is the termination, and Ft is the Ft correction.
954 *: These samples are also dated by the ZHe method.
955 +: Grain DC01-C is not used in the later analysis since its age is older than the Taiwan Orogeny.
956

957 Table 2. Additional published ZFT and ZHe ages used in this study.

| Sample | Location | | Altitude | Age ($\pm 1\sigma$) |
|---|---|---|---|---|
| | Lon ($°E$) | Lat ($°N$) | ($m$) | ($Ma$) |
| ZHe | | | | |
| C02-41[ξ] | 121.154 | 24.250 | 1487 | 1.46 (±0.10) |
| C04-03[ξ] | 121.115 | 24.253 | 1308 | 1.49 (±0.14) |
| C04-18[ξ] | 121.091 | 24.252 | 1039 | 1.51 (±0.02) |
| ZFT | | | | |
| CH-308[§] | 121.132 | 24.251 | 1445 | 2.9 (±0.5) |
| Beikou_23[†] | 121.130 | 24.195 | 2820 | 4.1 (±0.3) |
| Beikoi_24[†] | 121.124 | 24.196 | 3037 | 3.9 (±0.3) |
| Beikou_28[†] | 121.140 | 24.195 | 2806 | 3.6 (±0.5) |
| Beikou_Mt[†] | 121.109 | 24.203 | 3310 | 4.8 (±0.4) |
| TC012[†] | 121.104 | 24.240 | 1100 | 2.6 (±0.2) |
| TC014[†] | 121.095 | 24.242 | 1000 | 2.8 (±0.2) |

958 [ξ]: *Beyssac et al.* (2007), [§]: *Liu et al.* (2001), and [†]: *Lee* (2015).

959

960 Table 3. Parameters of the thermal models.

| Series | $t_m$ | $t_f$ | $r_m$ | $R_f$ | Lowest-misfit model | | | | |
|---|---|---|---|---|---|---|---|---|---|
| # | (Myr) | (Myr) | ($R_m/R_f$) | (km/Myr) | $R_f$ (km/Myr) | $\Delta R$ | $R_{avg}$ (km/Myr) | $G_t$ (°C/km) | s |
| 1(A)[ξ†] | - | 6 | - | 1.00-3.50 | 3.30 | 0.0606 | 3.3 | 13.66 | 5.042 |
| 2 | - | 7 | - | 1.00-3.50 | 1.90 | 0.0902 | 1.9 | 33.45 | 5.835 |
| 3 | 1 | 6 | 0.1 | 2.14-7.50 | 2.79 | 0.1538 | 1.3 | 33.45 | 4.758 |
| 4 | 1 | 6 | 0.2 | 1.94-6.77 | 2.90 | 0.1333 | 1.5 | 28.97 | 2.781 |
| 5 | 1 | 6 | 0.3 | 1.76-6.18 | 3.53 | 0.1000 | 2.0 | 20.49 | 1.780 |
| 6(B)[ξ†] | 1 | 6 | 0.4 | 1.62-5.68 | 3.73 | 0.0870 | 2.3 | 17.47 | 1.428 |
| 7 | 1 | 6 | 0.5 | 1.50-5.25 | 4.05 | 0.0741 | 2.7 | 14.49 | 1.518 |
| 8 | 1 | 6 | 0.6 | 1.40-4.88 | 4.19 | 0.0667 | 3.0 | 12.96 | 1.793 |
| 9 | 1 | 6 | 0.7 | 1.30-4.57 | 3.91 | 0.0667 | 3.0 | 13.29 | 2.340 |
| 10 | 1 | 6 | 0.8 | 1.22-4.29 | 3.92 | 0.0625 | 3.2 | 12.64 | 2.886 |
| 11 | 1 | 6 | 0.9 | 1.15-4.04 | 3.81 | 0.0606 | 3.3 | 12.35 | 3.378 |
| 12 | 1 | 6 | 1.0 | 1.09-3.82 | 3.60 | 0.0606 | 3.3 | 12.64 | 4.161 |
| 13 | 2 | 6 | 0.1 | 2.61-9.13 | 4.17 | 0.1250 | 1.6 | 25.91 | 43.84 |
| 14 | 2 | 6 | 0.2 | 2.31-8.08 | 3.00 | 0.1538 | 1.3 | 33.45 | 8.927 |
| 15 | 2 | 6 | 0.3 | 2.07-7.24 | 3.31 | 0.1250 | 1.6 | 25.91 | 4.400 |
| 16 | 2 | 6 | 0.4 | 1.88-6.56 | 4.12 | 0.0909 | 2.2 | 17.47 | 3.089 |
| 17 | 2 | 6 | 0.5 | 1.71-6.00 | 3.60 | 0.0952 | 2.1 | 19.31 | 1.480 |
| 18 | 2 | 6 | 0.6 | 1.58-5.53 | 3.63 | 0.0870 | 2.3 | 17.47 | 1.515 |
| 19 | 2 | 6 | 0.7 | 1.46-5.12 | 4.10 | 0.0714 | 2.8 | 13.66 | 1.702 |
| 20 | 2 | 6 | 0.8 | 1.36-4.77 | 3.95 | 0.0690 | 2.9 | 13.29 | 2.036 |
| 21 | 2 | 6 | 0.9 | 1.28-4.47 | 3.70 | 0.0690 | 2.9 | 13.66 | 2.710 |
| 22 | 2 | 6 | 1.0 | 1.20-4.20 | 3.48 | 0.0690 | 2.9 | 14.05 | 3.318 |
| 23 | 2 | 6 | 1.1 | 1.13-3.96 | 3.40 | 0.0667 | 3.0 | 13.66 | 3.861 |
| 24 | 2 | 6 | 1.2 | 1.07-3.75 | 3.43 | 0.0625 | 3.2 | 12.64 | 4.388 |
| 25 | 2 | 6 | 1.3 | 1.02-3.56 | 3.36 | 0.0606 | 3.3 | 12.35 | 4.935 |
| 26 | 2 | 6 | 1.4 | 0.97-3.39 | 3.19 | 0.0606 | 3.3 | 12.64 | 5.449 |
| 27 | 3 | 6 | 0.1 | 3.33-11.7 | 3.33 | 0.2000 | 1.0 | 57.94 | 96.24 |
| 28 | 3 | 6 | 0.2 | 2.86-10.0 | 4.57 | 0.1250 | 1.6 | 25.91 | 63.59 |
| 29 | 3 | 6 | 0.3 | 2.50-8.75 | 3.25 | 0.1538 | 1.3 | 33.45 | 16.53 |
| 30 | 3 | 6 | 0.4 | 2.22-7.78 | 2.89 | 0.1538 | 1.3 | 33.45 | 5.988s |
| 31 | 3 | 6 | 0.5 | 2.00-7.00 | 3.20 | 0.1250 | 1.6 | 25.91 | 3.203 |
| 32 | 3 | 6 | 0.6 | 1.82-6.36 | 4.00 | 0.0909 | 2.2 | 17.47 | 2.694 |
| 33 | 3 | 6 | 0.7 | 1.67-5.83 | 3.50 | 0.0952 | 2.1 | 19.31 | 1.534 |
| 34 | 3 | 6 | 0.8 | 1.54-5.38 | 3.85 | 0.0800 | 2.5 | 15.49 | 1.649 |
| 35 | 3 | 6 | 0.9 | 1.43-5.00 | 3.71 | 0.0769 | 2.6 | 14.96 | 1.830 |
| 36 | 3 | 6 | 1.0 | 1.33-4.67 | 3.73 | 0.0714 | 2.8 | 13.66 | 2.036 |
| 37 | 3 | 6 | 1.1 | 1.25-4.38 | 3.62 | 0.0690 | 2.9 | 13.29 | 2.478 |
| 38 | 3 | 6 | 1.2 | 1.18-4.12 | 3.65 | 0.0645 | 3.1 | 12.35 | 2.962 |
| 39 | 3 | 6 | 1.3 | 1.11-3.89 | 3.44 | 0.0645 | 3.1 | 12.35 | 3.585 |
| 40 | 3 | 6 | 1.4 | 1.05-3.68 | 3.26 | 0.0645 | 3.1 | 12.64 | 4.084 |
| 41(D)[†] | 4 | 6 | 0.3 | 3.16-11.1 | 3.16 | 0.2000 | 1.0 | 57.94 | 62.44 |
| 42 | 4 | 6 | 0.4 | 2.73-9.55 | 3.55 | 0.1538 | 1.3 | 33.45 | 20.77 |
| 43 | 4 | 6 | 0.5 | 2.40-8.40 | 3.12 | 0.1538 | 1.3 | 33.45 | 7.984 |
| 44 | 4 | 6 | 0.6 | 2.14-7.50 | 3.43 | 0.1250 | 1.6 | 25.91 | 4.126 |
| 45 | 4 | 6 | 0.7 | 1.94-6.77 | 2.90 | 0.1333 | 1.5 | 28.97 | 2.837 |
| 46 | 4 | 6 | 0.8 | 1.76-6.18 | 2.47 | 0.1429 | 1.4 | 33.45 | 2.505 |
| 47 | 4 | 6 | 0.9 | 1.62-5.68 | 3.57 | 0.0909 | 2.2 | 17.47 | 1.914 |
| 48 | 4 | 6 | 1.0 | 1.50-5.25 | 3.15 | 0.0952 | 2.1 | 19.31 | 1.630 |
| 49 | 4 | 6 | 1.1 | 1.40-4.88 | 3.35 | 0.0833 | 2.4 | 16.07 | 1.755 |
| 50 | 4 | 6 | 1.2 | 1.30-4.57 | 3.26 | 0.0800 | 2.5 | 15.49 | 1.969 |
| 51 | 4 | 6 | 1.3 | 1.22-4.29 | 3.31 | 0.0741 | 2.7 | 14.05 | 2.100 |
| 52 | 4 | 6 | 1.4 | 1.15-4.04 | 3.12 | 0.0741 | 2.7 | 14.05 | 2.218 |
| 53 | 5 | 6 | 0.4 | 3.53-12.4 | 5.65 | 0.1250 | 1.6 | 25.91 | 34.76 |
| 54 | 5 | 6 | 0.5 | 3.00-10.5 | 3.90 | 0.1538 | 1.3 | 33.45 | 9.553 |
| 55 | 5 | 6 | 0.6 | 2.61-9.13 | 3.39 | 0.1538 | 1.3 | 33.45 | 6.027 |
| 56 | 5 | 6 | 0.7 | 2.31-8.08 | 3.69 | 0.1250 | 1.6 | 25.91 | 4.687 |
| 57 | 5 | 6 | 0.9 | 1.88-6.56 | 2.81 | 0.1333 | 1.5 | 28.97 | 2.737 |
| 58 | 5 | 6 | 1.0 | 1.71-6.00 | 2.57 | 0.1333 | 1.5 | 28.97 | 2.539 |
| 59 | 5 | 6 | 1.1 | 1.58-5.53 | 2.37 | 0.1333 | 1.5 | 28.97 | 2.686 |
| 60 | 5 | 6 | 1.2 | 1.46-5.12 | 2.05 | 0.1429 | 1.4 | 33.45 | 2.465 |
| 61 | 5 | 6 | 1.3 | 1.36-4.77 | 3.00 | 0.0909 | 2.2 | 17.47 | 2.551 |

961 For all series, $R_{avg}$ values are 1.0-3.5 km/Myr, the initial thermal ages are 5-110 Ma, and $G_t$
962 values are 12.35-57.84°C/km. [ξ]: The misfits of these series, with varying $G_t$ and $R_{avg}$ values,
963 are shown in Fig. 6. [†]: The lowest-misfit models of these series are labeled in Fig. 7.

964 Table 3. Parameters of the thermal models (continue)

| Series | $t_m$ | $t_f$ | $r_m$ | $R_f$ | Lowest-misfit model | | | | |
|---|---|---|---|---|---|---|---|---|---|
| # | (Myr) | (Myr) | ($R_m/R_f$) | (km/Myr) | $R_f$ (km/Myr) | $\Delta R$ | $R_{avg}$ (km/Myr) | $G_t$ (°C/km) | s |
| 62 | 1 | 7 | 0.1 | 2.09-7.31 | 3.76 | 0.0952 | 1.8 | 19.31 | 2.089 |
| 63 | 1 | 7 | 0.2 | 1.89-6.62 | 3.41 | 0.0952 | 1.8 | 20.49 | 1.639 |
| 64 | 1 | 7 | 0.3 | 1.73-6.05 | 4.15 | 0.0714 | 2.4 | 14.49 | 1.517 |
| 65 | 1 | 7 | 0.4 | 1.59-5.57 | 4.30 | 0.0635 | 2.7 | 12.64 | 1.772 |
| 66 | 1 | 7 | 0.5 | 1.47-5.16 | 4.13 | 0.0612 | 2.8 | 12.64 | 2.181 |
| 67 | 1 | 7 | 0.6 | 1.37-4.80 | 3.57 | 0.0659 | 2.6 | 14.49 | 3.063 |
| 68 | 1 | 7 | 0.7 | 1.28-4.50 | 3.85 | 0.0571 | 3.0 | 12.35 | 3.588 |
| 69 | 1 | 7 | 0.8 | 1.21-4.22 | 3.38 | 0.0612 | 2.8 | 14.05 | 4.241 |
| 70 | 1 | 7 | 0.9 | 1.14-3.98 | 3.07 | 0.0635 | 2.7 | 15.49 | 4.987 |
| 71 | 1 | 7 | 1.0 | 1.08-3.77 | 3.34 | 0.0553 | 3.1 | 12.96 | 5.526 |
| 71(A')* | 1 | 7 | 1.0 | 3.23 | 3.23 | 0.0571 | 3.0 | 13.66 | 5.751 |
| 72 | 2 | 7 | 0.1 | 2.46-8.60 | 2.95 | 0.1429 | 1.2 | 33.45 | 6.161 |
| 73 | 2 | 7 | 0.2 | 2.19-7.66 | 3.72 | 0.1008 | 1.7 | 20.49 | 2.913 |
| 74 | 2 | 7 | 0.4 | 1.79-6.28 | 3.59 | 0.0857 | 2.0 | 18.32 | 1.513 |
| 75 | 2 | 7 | 0.5 | 1.65-5.76 | 3.95 | 0.0714 | 2.4 | 14.49 | 1.804 |
| 76 | 2 | 7 | 0.6 | 1.52-5.33 | 3.96 | 0.0659 | 2.6 | 13.66 | 2.071 |
| 77 | 2 | 7 | 0.7 | 1.41-4.95 | 3.96 | 0.0612 | 2.8 | 12.64 | 2.626 |
| 78 | 2 | 7 | 0.8 | 1.32-4.62 | 3.83 | 0.0591 | 2.9 | 12.35 | 3.405 |
| 79 | 2 | 7 | 0.9 | 1.24-4.34 | 3.59 | 0.0591 | 2.9 | 12.96 | 4.258 |
| 80 | 2 | 7 | 1.0 | 1.17-4.08 | 3.38 | 0.0591 | 2.9 | 13.29 | 4.874 |
| 81 | 2 | 7 | 1.1 | 1.10-3.86 | 3.42 | 0.0553 | 3.1 | 12.35 | 5.461 |
| 82 | 3 | 7 | 0.2 | 2.59-9.07 | 2.59 | 0.1714 | 1.0 | 40.97 | 7.816 |
| 83 | 3 | 7 | 0.3 | 2.30-8.03 | 3.67 | 0.1071 | 1.6 | 21.90 | 4.050 |
| 84 | 3 | 7 | 0.4 | 2.06-7.21 | 3.09 | 0.1143 | 1.5 | 25.91 | 2.086 |
| 85 | 3 | 7 | 0.5 | 1.87-6.53 | 4.11 | 0.0779 | 2.2 | 15.49 | 1.543 |
| 86 | 3 | 7 | 0.6 | 1.71-5.98 | 3.76 | 0.0779 | 2.2 | 16.07 | 1.537 |
| 87 | 3 | 7 | 0.7 | 1.57-5.51 | 4.25 | 0.0635 | 2.7 | 12.35 | 1.934 |
| 88 | 3 | 7 | 0.8 | 1.46-5.10 | 3.79 | 0.0659 | 2.6 | 13.66 | 2.564 |
| 89 | 3 | 7 | 0.9 | 1.36-4.76 | 3.81 | 0.0612 | 2.8 | 12.64 | 3.213 |
| 90 | 3 | 7 | 1.0 | 1.27-4.45 | 4.25 | 0.0591 | 2.7 | 12.35 | 3.950 |
| 91 | 3 | 7 | 1.1 | 1.20-4.19 | 3.47 | 0.0591 | 2.9 | 12.64 | 4.624 |
| 92 | 3 | 7 | 1.2 | 1.13-3.95 | 3.27 | 0.0591 | 2.9 | 12.96 | 5.365 |
| 93 | 3 | 7 | 1.3 | 1.07-3.74 | 3.21 | 0.0571 | 3.0 | 12.64 | 5.960 |
| 94 | 3.5 | 7 | 0.5 | 2.00-7.00 | 3.40 | 0.1008 | 1.7 | 21.90 | 1.708 |
| 95 | 4 | 7 | 0.3 | 2.75-9.61 | 2.75 | 0.1714 | 1.0 | 40.97 | 10.37 |
| 96 | 4 | 7 | 0.4 | 2.41-8.45 | 2.90 | 0.1429 | 1.2 | 33.45 | 4.617 |
| 97 | 4 | 7 | 0.5 | 2.15-7.54 | 3.88 | 0.0952 | 1.8 | 19.31 | 2.758 |
| 98 | 4 | 7 | 0.6 | 1.94-6.81 | 3.89 | 0.0857 | 2.0 | 17.47 | 1.704 |
| 99 | 4 | 7 | 0.7 | 1.77-6.20 | 3.72 | 0.0816 | 2.1 | 16.73 | 1.538 |
| 100 | 4 | 7 | 0.8 | 1.63-5.70 | 3.74 | 0.0745 | 2.3 | 14.96 | 1.938 |
| 101 | 4 | 7 | 0.9 | 1.51-5.27 | 3.91 | 0.0659 | 2.6 | 12.96 | 2.166 |
| 102 | 4 | 7 | 1.0 | 1.40-4.90 | 3.64 | 0.0659 | 2.6 | 13.29 | 2.729 |
| 103 | 4 | 7 | 1.1 | 1.31-4.58 | 3.66 | 0.0612 | 2.8 | 12.35 | 3.380 |
| 104 | 4 | 7 | 1.2 | 1.23-4.30 | 3.44 | 0.0612 | 2.8 | 12.64 | 4.133 |
| 105 | 4 | 7 | 1.3 | 1.16-4.05 | 3.24 | 0.0612 | 2.8 | 12.96 | 4.999 |
| 106 | 4 | 7 | 1.4 | 1.09-3.83 | 3.17 | 0.0591 | 2.9 | 12.35 | 5.312 |
| 107 | 5 | 7 | 0.5 | 2.55-8.91 | 3.82 | 0.1143 | 1.5 | 23.65 | 5.310 |
| 108 | 5 | 7 | 0.6 | 2.26-7.90 | 4.06 | 0.0952 | 1.8 | 19.31 | 3.328 |
| 109 | 5 | 7 | 0.8 | 1.84-6.45 | 3.68 | 0.0857 | 2.0 | 17.47 | 1.487 |
| 110 | 5 | 7 | 0.9 | 1.69-5.90 | 3.54 | 0.0816 | 2.1 | 16.73 | 1.603 |
| 111 | 5 | 7 | 1.0 | 1.56-5.44 | 3.73 | 0.0714 | 2.4 | 14.05 | 1.757 |
| 112 | 5 | 7 | 1.1 | 1.44-5.05 | 3.75 | 0.0659 | 2.6 | 12.64 | 2.157 |
| 113 | 5 | 7 | 1.2 | 1.35-4.71 | 3.50 | 0.0659 | 2.6 | 12.96 | 2.304 |
| 114 | 5 | 7 | 1.3 | 1.26-4.41 | 3.41 | 0.0635 | 2.7 | 12.35 | 2.723 |
| 115 | 6 | 7 | 0.6 | 2.69-9.42 | 4.58 | 0.1008 | 1.7 | 20.49 | 3.359 |
| 116 | 6 | 7 | 0.7 | 2.37-8.31 | 4.27 | 0.0952 | 1.8 | 19.31 | 2.389 |
| 117 | 6 | 7 | 0.8 | 2.12-7.42 | 3.39 | 0.1071 | 1.6 | 23.65 | 1.957 |
| 118 | 6 | 7 | 0.9 | 1.92-6.71 | 3.64 | 0.0902 | 1.9 | 18.32 | 1.776 |
| 119 | 6 | 7 | 1.0 | 1.75-6.12 | 3.15 | 0.0952 | 1.8 | 20.49 | 1.558 |
| 120(C)† | 6 | 7 | 1.1 | 1.61-5.63 | 3.22 | 0.0857 | 2.0 | 17.47 | 1.532 |
| 121 | 6 | 7 | 1.2 | 1.49-5.21 | 3.28 | 0.0779 | 2.2 | 15.49 | 1.592 |
| 122 | 6 | 7 | 1.3 | 1.39-4.85 | 2.91 | 0.0816 | 2.1 | 16.73 | 1.548 |
| 123 | 6 | 7 | 1.4 | 1.30-4.54 | 2.72 | 0.0816 | 2.1 | 16.73 | 1.559 |
| 124 | 6 | 7 | 1.5 | 1.22-4.26 | 2.56 | 0.0816 | 2.1 | 16.73 | 1.662 |

965 *: This model in Series 71 (Model A') is for the comparison with Model A, which has the

966 same Gt and 2% lower $R_f$ than that of Model A.